DEM simulation of mortar-bolt interface behaviour subjected to shearing

J Shang [a], Y Yokota [a,b], Z Zhao [a], W Dang [c]

[a] Nanyang Centre for Underground Space, School of Civil and Environmental Engineering, Nanyang Technological University, Singapore

[b] Kajima Technical Research Institute, Kajima Corporation, Japan

[c] Institute of Geotechnics, TU Bergakademie Freiberg, Freiberg, Germany

Keywords: Cement mortar; rebar bolt; direct shear; mortar rupture; discrete element method

Received 1 March 2018, Revised 9 June 2018, Accepted 9 July 2018,

Please cite this paper as: **Shang J, Yokota Y, Zhao Z, Dang W. DEM simulation of motar-bolt interface behaviour subjected to shearing. Construction and Building Materials 185: 120-137. https://doi.org/10.1016/j.conbuildmat.2018.07.044**

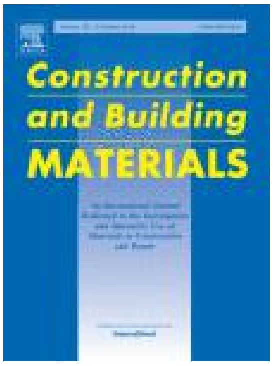

Highlights

1. A DEM model was established to investigate the micro-macro behaviours of mortar-bolt interface subjected to shearing.

2. This study allows detailed observations of mortar-bolt interface debonding and mortar rupture.

3. The effects of particle size distribution and bolt profile configuration on simulation results were discussed.

4. The simulation results were validated against experimental measurements.

Abstract

In this study, a 3D DEM model containing a mortar-bolt interface subjected to shearing was established in the context of the simplified rock bolt model (SRBM) proposed in a companion paper. The DEM model was calibrated against a series of laboratory experiments to reproduce the mechanical characteristics of a cement mortar with a uniaxial compressive strength of 30 MPa. The DEM simulation has led to a detailed observation and an in-depth understanding of the mode II progressive debonding of the mortar-bolt interface and subsequent mortar rupture (due to mechanical interlocking). In addition, the effects of particle size of mortar and profile configurations of rebar bolts (i.e., different rib spacings and rib heights) on simulation results were discussed. The numerical findings in the study were validated against laboratory measurements and a broad agreement was observed.

1. Introduction

Fully grouted rebar bolts have been widely used in the support of fractured rock masses in civil and mining engineering applications due to their proven efficacy and relatively low costs. The inherent strength of a fractured rock mass can be dramatically improved if a suitable rebar bolt is selected and properly installed [1]. Rock bolting has been of interest to practitioners and academics and has thus been studied for quite some time. It is well accepted that the supporting capacity of a fully grouted rebar bolt is largely dominated by its load transfer capacity, which relies on the shear strength of the mortar-bolt or mortar-rock interface and the mechanical interlocking between mortar and bolt ribs [2,3].

Laboratory and in-situ pull-out experiments are often conducted to understand the rock bolting mechanism [1,2, 4–9]. It has been identified that debonding failure of the mortar-bolt interface often occurred for a fully grouted rock bolt, which is mainly due to the lower adhesive strength of the mortar-bolt interface in comparison with that of the mortar-rock interface. Fig. 1 presents a laboratory-reproduced example of the debonding failure of a mortar-bolt interface. Nevertheless, the progressive debonding process and subsequent mortar-bolt interactions which are not readily achievable and observable in current experimentation are still not well understood, although some attempts exist [5,10]. It is therefore imperative to investigate the micro-mechanism underlying the mortar-bolt interactions subjected to shearing.

In the past decades, some analytical models have been developed to investigate the mortar-bolt interactions, including the well-known bond strength model (BSM) [11], tri-linear bond-slip model (TLBSM) [12] and interfacial shear stress model (ISSM) [13]. Ren et al. [14] proposed a closed-form solution for a better understanding of the debonding mechanism of the mortar-bolt interface. Ma et al. [15] presented an analytical model for a further understanding of the mechanical interaction at the mortar-bolt interface. Cao et al. [2] analytically investigated two major failure modes (i.e., parallel shear failure and dilational slip failure) that often occurred at the mortar-bolt interface. Although those analytical studies have led to a deeper understanding of the rock bolting mechanism, they largely ignored the influence of profile configuration of rebar bolts, which is fundamentally important to the supporting capacity (in the sense of the mechanical interlocking) of a rock bolting system [2]. Additionally, the existing analytical models are unable to account for three-dimensional deformation of bonding materials (i.e., mortar), which is also important for a realistic understanding of the mortar-bolt interaction mechanism.

To date both continuum-based numerical methods [16–19] and discontinuum-based numerical methods [20–22] have been used in the numerical study of mortar-bolt interactions. For example, Li [23] investigated the interactions between steel bolt and concrete based on the finite element analysis, ABAQUS. He et al. [17] proposed and implemented a unified rock bolt model (URBM) into the two-dimensional discontinuous deformation analysis (DDA). The URBM can simulate the debonding process of the mortar-bolt and mortar-rock interfaces at large displacement although the accuracy is mesh-dependent due to the DDA code. Wang et al. [24] investigated the micro-macro failure mechanisms of a bolted joint using the discrete element method (particle flow code 2D). The continuum-based numerical methods have the limitation of investigating micromechanical behaviour of a rock or a solid material, thus the micro-mechanisms underlying the failure process cannot be known [25]. On the contrary, discontinuum-based numerical methods allow an explicit investigation and observation of the micro-crack initiation and propagation, which are more suitable for capturing the micromechanical behaviour of a rock bolting system.

There exist several models which are based on the Discrete Element Method (DEM) for investigating the micro-macro behaviours of solid materials, for example the Universal Distinct Element Code (UDEC), the Particle Flow Code (PFC), and YADE. The DEM is a discontinuum-based numerical technique that defines solid materials as rigid blocks or particles. Comparing with the block-based DEM (such as UDEC), the particle-based DEM (such as PFC and YADE) discretizes solid materials as rigid particles through which the number of degrees of freedom can be decreased, thereby increasing the computational efficiency [26]. The PFC has some additional advantages over other particle-based DEM models. First, it can conveniently model fracture initiation and propagation; moreover it has resolved the intrinsic limitation of the particle-based DEM models (i.e., the low compression-to-tensile strength ratio due to the inadequate interlocking between spherical particles) by implementing the Flat Joint Contact Model (FJCM) which can provide efficient grain interlocking [26]. Furthermore, the PFC allows a detailed description of the interface/joint sliding behaviour by implementing the Smooth Joint Contact Model (SJCM). See a further discussion on this point in Section 3.1. Hitherto the PFC has been widely used in the investigation of the micro-macro failure mechanisms of solid materials, including anisotropic rocks [27], coal [28], porous concrete [29,30] and cement mortar [31,32]. As such, the PFC was used in the present study to investigate the mortar-bolt interface behaviour.

The primary aim of the study is to explore the micro-mechanisms underlying the mortar-bolt interactions. A DEM model was constructed based on three main assumptions: (1) the bond strength of mortar-rock interface is much stronger than that of mortar-bolt interface; (2) the possible chemical effect of the cement composition on the micro-structure of the steel bolt surface is ignored for simplification; and (3) the elongation and twisting of the rebar bolt are not considered (see detailed discussion on these assumptions in the Discussion section). The DEM model was calibrated against a series of laboratory experiments on a cement mortar to reproduce its mechanical characteristics. Simulated results based on the DEM model have been validated against laboratory measurements. This study allows a combined micro- and macro-scale observation of mode II progressive debonding of the mortar-bolt interface and subsequent rupture of the mortar (due to mechanical interlocking).

2. Laboratory experiment

A simplified rock bolt model (SRBM) was recently proposed by Yokota et al. [33] to investigate the mechanical and deformable behaviours of mortar-bolt interfaces in the laboratory. Fig. 2b shows a schematic diagram of the SRBM from a portion of a fully grouted rebar bolt. In the SRBM, the dark area on the bottom represents a small section of the rebar bolt (Fig. 2b), while the light area stands for the mortar. The terminologies for the profile configuration of the rebar bolt are included in Fig. 2b. In the experiment, the rebar bolt deformed along the direction as shown by the red arrows and the mortar was fixed. The simulation performed in this study is aimed at exploring a further understanding of the laboratory experiments performed on the SRBM in a direct shear configuration [33]. For clarification, in this section, the sample preparation and experimental setup procedures are briefly reviewed.

In the laboratory setup, block samples with three different rib angles (i.e., β=30°, 60° and 90°, respectively, see Fig. 3) were prepared and each sample comprised of a cement mortar (top) and a rebar bolt (bottom). The mortar used in the samples was a mixture of sand (the grain size ranges from 0.2 to 0.3 mm), cement, additive and water with a ratio of 10:9:1:6.5 by weight. The mixing and casting processes were carefully controlled and the casted mortar samples were left at room temperature for 15 days to make sure that the mortar samples have identical mechanical properties. Some of the mechanical properties of the mortar are listed in Table 1. The rebar bolts (steel blocks in Fig. 3) were specially manufactured for the experiments and their profile configurations were determined according to the specifications of the rebar bolts typically used in Japan [33]. As shown in Fig. 3, the rib height (R_h) and rib spacing (R_s) of all tested laboratory samples remain constant, which are 2 and 17.8 mm, respectively; while the average rib width (R_w) varied with the rib angles. A portable shear box (model: PHI-10) was used in the direct shear tests and illustrated schematically in Fig. 4. A vertical load was applied on the top by a hydraulic jack and it was kept constant during the test. A shear load was applied at a constant velocity of 0.1 mm/s at the bottom of shear box by another hydraulic jack. Two linear variable differential transformers (LVDT) were installed to measure the vertical and horizontal displacements. A high-speed and compact camera was used to capture the failure processes of the mortar samples in the experiment. Tests were conducted up to a normal stress of 4 MPa that is the equivalent of 150~200 m of rock, which therefore is adequate for most civil engineering projects [34].

The laboratory investigation revealed the macro-failure mechanism of the mortar-bolt interface under direct shear and captured the failure process of the mortar from the sample appearance [33]. As discussed in Introduction, it is also important to understand the micro-failure mechanism underlying the experimental observations, which are not achievable from the current laboratory study. A numerical study is therefore presented in the following sections to facilitate a deeper understanding of the mortar-bolt interactions, thereafter improving the bolt profile optimisation.

3. DEM model establishment

3.1 The Particle Flow Code and contact models used in the study

The Particle Flow Code (PFC 3D), which implements the DEM technique, was used in this study. In PFC 3D, the micro-structure of a solid material is constructed and represented by an assembly of rigid particles that are bonded (cemented) together at their contacts [35].

To date two types of bonded contacts are available in PFC 3D, i.e., the Linear Parallel Bond Contact Model (LPBCM, see Fig. 5a) and the Flat Joint Contact Model (FJCM, see Fig. 5b). The main difference between these two types of contacts arises from the way of interface connecting between adjacent spherical particles. The LPBCM (also termed as the Standard Bonded Particle Model, SBPM) represents the interfacial connect as a single bond element at the entire interface and the interface will vanish after the bond breakage (see the orange parallel bonds in Fig. 5a). The mechanism of force and moment of LPBCM is described by Eqs. 1 to 4.

$$\Delta F_n = k_n A \Delta \partial_n \tag{1}$$

$$\Delta F_s = -\, k_s A \Delta \partial_s \tag{2}$$

$$\Delta M_n = -\, k_n J \Delta \theta_n \tag{3}$$

$$\Delta M_s = -\, k_s\, I \Delta \theta_s \tag{4}$$

where ΔF_n and ΔF_s are increments of normal and shear forces and F_n>0 is tension. ΔM_n and ΔM_s are increments of components of parallel-bond moment; k_n and k_s are normal and shear stiffness of the parallel bond; $\Delta\partial_n$ and $\Delta\partial_s$ are increments of normal and shear displacement, respectively; J and I are polar moment and moment of the cross section of parallel bond and A is the cross-sectional area of bond. The tensile and shear strength of the parallel-bond can be calculated using Eqs. 5 and 6. The parallel bond will break if applied stresses exceed the tensile or shear strength of bond, thus failure of rock can be simulated in either tension or shear.

$$\sigma = \frac{F_n}{A} + K\frac{|M_s|R}{I} \quad (5)$$

$$\tau = \frac{F_s}{A} + K\frac{|M_n|R}{J} \quad \text{(3D)} \quad (6)$$

where σ and τ are tensile and shear stresses of the parallel-bond periphery; R is a bond cross-sectional property (shown in Fig. 3a). K is the moment-contribution factor to strength, see [35] for more details.

For the FJCM, a planar interface with several elements is used which allows partial damage, after which the interface still exists (see the 3D flat interface in Fig. 5b). Each element bears a force (F_e) and moment (M_e) acting at the element centroid. The force acting on one element can be resolved into a normal (F_e^n) and shear force (F_e^s), which are given by Eq. 7

$$F_e = -F_e^n n_c + F_e^s \quad (7)$$

where $F_e^n > 0$ is tension and n_c is a unit vector.

The element normal (σ_e^n) and shear (τ_e^n) stresses are therefore can be described by Eqs. 8 and 9.

$$\sigma_e^n = {F_e^n}/{A_e} \quad (8)$$

$$\tau_e^n = {F_e^s}/{A_e} \quad (9)$$

where A_e is the area of the element.

The element will break either in tension or shear if applied stresses exceed the tensile or shear strength of element bond. See [36] for a detailed comparison of the SBPM and FLCM.

Since 2004, the SBPM has been widely used in the past studies [27,28,35]; although successful, this contact model suffers from a major intrinsic problem, which has been realised by many researchers, such as Wu and Xu [36] and Vallejos et al. [37]. The major problem is that the spherical particles cannot provide adequate grain interlocking (after the parallel bond was broken and vanished) as that of real solid materials like rock, see [36] for more discussions on this topic. To represent a larger friction and simulate realistic grain interlocking, in past studies, the value of the particle friction was set relatively larger, sometimes more than 1.0 [38, 39] and even larger [40]. This routine leads to a very low compressive-to-tensile strength ratio (often less than 4.0), which is unrealistic for brittle solid materials like high-strength cement mortars and brittle rocks. The FJCM can resolve this issue to a large extent thanks to the partially damaged interfaces which are able to provide much more interlocking between particles, as discussed earlier. Potyondy [41] and Vallejos et al. [37] demonstrated that the calculated compressive-to-tensile strength ratio based on the FJCM is able to match that of experimental results. In this study, to ensure a realistic reproduction of the mechanical characteristics of the cement mortar, the FJCM was selected for connecting the spherical particles of the cement mortar and the SBPM (i.e., LPBCM) was used to simulate the steel rebar bolt for simplification, since it is assumed that the bolt is non-breakable and non-elongatable in the study (Section 1).

Apart from the above two bonded particle models, the Smooth Joint Contact Model (SJCM) and the Linear Model (LM) are also used in the DEM model establishment. In the SJCM, smooth-jointed particles lying upon opposite sides of a joint can overlap and slide past each other (Fig. 5c). The SJCM was assigned to the mortar-bolt interface to eliminate the unrealistic dilation arising from spherical particles. The LM was assigned between particles and walls.

3.2 DEM model setup

Fig. 6 shows a representative setup of the DEM model of the direct shear test (rib angle β =90°). As shown in Fig. 6a, the three-dimensional DEM model had dimensions of 80 mm X 80 mm X 24 mm (the same as that of the laboratory setup). The rib profile is the same as that of the laboratory sample (Fig. 3c). Cement mortars with a minimum particle radius of 0.6 mm and a particle size ratio (d_{max}/d_{min}) of 1.5 were produced on the top (green particles in Fig. 6a), which satisfies a uniform particle size distribution [27]. Considering the small size of the bolt ribs used in the laboratory experiment, uniformly distributed particles with somewhat smaller particle sizes (radii varying from 0.4 to 0.6 mm) were generated at the bottom of the mortar to represent a rebar bolt (grey particles in Fig. 6a). The mortar comprised of around 30000 particles (green particles in Fig. 6a), which is sufficient to reproduce failure mechanisms. The generated DEM model was surrounded by a series of walls (periodic boundary) forming the top shear box (purple in Fig. 6a) and the bottom shear box (red in Fig. 6a), respectively. Note that two walls in the front are not shown in Fig. 6a for clarity. Fig. 6b shows a close-up view of the mortar-bolt interface and the profile configuration values of the rebar bolt are included. A total of 843222 contacts with four different contact models (as described in Section 3.1) were created in the DEM model. Fig 6c shows a section of the contacts where the LM without contact friction was assigned between particles and walls; the FJCM was used to represent the cement mortar on the top; the LPBCM was used to generate the rebar bolt on the bottom; and the SJCM was assigned between particles forming the mortar-bolt interface. For clarity, contacts are shown as coloured cylinders without showing particles and walls.

In the simulation, the bottom shear box was moved at a constant velocity of 0.02 m/s (see the red arrow in Fig. 6a), which is small enough for maintaining a static equilibrium during shear [40]. While the top box (purple in Fig. 6a) was fixed and a normal load was applied on the top and kept constant during shear using the servo mechanism [41, 42]. Numerical simulation was terminated when the horizontal displacement of the bottom shear box reached 8 mm (10% the sample length).

4. Calibration and verification of the DEM model

Unconfined compression tests, triaxial compression tests and Brazilian tests were conducted on the cement mortar for calibrating and verifying the FJCM and the LM, followed by the selection of the micro-parameters for the LPBCM (assigned for the rebar bolts). The mortar-bolt interface properties (with the SJCM) were calibrated against direct shear and normal deformability tests on mortar-bolt interfaces.

4.1 Calibration and verification of the FJCM for the cement mortar

To calibrate the FJCM, a DEM cylindrical sample (with the FJCM) containing 15038 particles with a radius between 0.6 and 0.9 mm was generated. The size of the DEM sample (80 mm X 40 mm) was the same as that of physical samples used in the laboratory. The Young's moduli of the particles and flat joint bond were firstly calibrated against the Young's modulus of the mortar measured in the uniaxial compression test, followed by the calibration of the normal-to-shear stiffness ratios of the linear contact and flat joint bond through matching the Poisson's ratio of the mortar. After that, the cohesion, tensile strength and friction coefficient of the flat joint bond were varied to match the average uniaxial compressive strength of the mortar (30.2 MPa, Table 1). Fig. 7a shows a comparison of the stress-strain curves from the laboratory experiments and the DEM simulation. As can be seen, the DEM result matched well with those results from the laboratory experiments, although a lack of agreement of the post-peak behaviour (i.e., brittleness) was observed. The DEM sample exhibited much more brittleness than that of the laboratory samples (except S4). A likely reason for the discrepancy is that the micro-cracks generated within the flat-jointed DEM model cannot coalesce easily and particle rotations were significantly suppressed due to the existence of the flat interfaces after bond failure [41], which will lead to a sudden failure of the DEM sample when the strength was reached.

The failure mode of the DEM sample under uniaxial compression (Fig. 7c) was similar to that of the physical samples used in the laboratory experiments (especially S4, Fig. 7b). Table 2 lists corresponding calibrated micro-parameters. Apart from the above micro-parameters (need calibration), in the FJCM, some parameters are determined based on specific situations [41]. In this study, the flat-joint bonded and gapped fraction were set to 1 and 0, respectively, to ensure that no initial cracks are inside of the cement mortar. Minimum values of the radial and circumferential elements (1 and 3, respectively) were used to reduce the calculation time [24].

To verify the reasonability of the compressive-to-tensile strength ratio and mechanical response of the cement mortar under confinements, the same DEM cylindrical samples with the micro-parameters listed in Table 2 were tested under splitting tension and triaxial compression. It is note that the splitting tensile tests were performed (at the Kajima research institute, Japan) because of the recognised difficulty in the setup of the direct tensile test [33, 43–45]. In the splitting tests, cylindrical samples with a diameter of 40 mm and a length of 80 mm were split along axes to measure the tensile strength, following the ASTM standards (C-496 and 192/C 192M) [46, 47]. A splitting tensile strength of 1.74 MPa was measured in the DEM simulation (Table 1), and a compressive-to-tensile strength ratio of 17.7 was calculated, which agreed well with that from the laboratory experiment (16.8).

DEM triaxial tests were performed under different confining pressures (CP=1.5, 3 and 6 MPa, respectively), which are the same to that of physical experiments. Fig. 8 presents a comparison between experimental results and numerical results. This figure demonstrates that the moduli and stresses from the numerical simulations are in broad agreements with those from the laboratory measurements. It is noted that the volumetric strain was not logged in the physical experiments as the triaxial tests on the mortar (a soft material) were conducted using a triaxial testing machine under undrained conditions (the apparatus is normally used for soil and soft materials).

4.2 Micro-parameter selection of the rebar bolt

As descripted in Section 2.1, the rebar bolt used in the study is assumed non-breakable and non-deformable as the UCS and modulus of the steel rebar bolt are much larger in comparison with that of the mortar used. The micro-parameters of the rebar bolt (see Table 3) were selected based on previous experience [27] and literature [24].

4.3 Calibration of the SJCM for the mortar-bolt interface

Calibration of the properties of the mortar-bot interface involved the calibration of the shear stiffness and friction coefficient of the SJCM against a laboratory direct shear test and the calibration of the normal stiffness against a normal deformability test.

In the laboratory experiment, a rock bolt sample without bolt ribs was used in the direct shear test. The mortar and mortar-bolt interface were carefully casted and prepared in the laboratory. The dimension of the sample (80 mm X 80 mm X 24 mm) was the same as those samples described in Fig. 3 and the shear test was performed firstly under a constant normal stress of 2 MPa using the same shear box (PHI-10) described in Section 2.2. The stress-displacement curve from the laboratory experiment is shown in Fig. 9a (back line) and this curve was used in the calibration of the shear stiffness. In the numerical simulation, a DEM sample having a width of 80 mm, length of 80 mm and height of 24 mm was generated and the radii of the mortar (0.4-0.6 mm) and the bolt (0.6-0.9 mm) are the same as those of the DEM sample described in Fig. 6a. The previously calibrated micro-parameters for the mortar and the bolt (Tables 2 and 3) were used in the DEM sample generation and the shear stiffness was then calibrated through a trial-and-error process. More direct shear tests were conducted on mortar-bolt interfaces under higher normal stresses (i.e., 4 and 6 MPa) and results were used to calibrate the smooth joint friction coefficient. Fig. 9a shows a comparison of the stress-displacement curves from the numerical and experimental tests under different normal stresses. The initial stress fluctuation observed in the laboratory tests (especially for 4 and 6 MPa, Fig. 9a) is likely due to the slight loose connection between the shear box and the mortar. But in general, acceptable agreements can be observed. In addition, the failure pattern of the DEM sample also agrees well that observed from the experiment (see Figs. 9b, 9c and 9d). No fractures were observed on the appearance of the mortar material after direct shear (Fig. 9b) and the simulation reproduced this macro-scale observation (Fig. 9c). Additionally, the particulate DEM simulation also provided some insights at the micro-scale level, which showed that shear micro-cracks (red) dominated on the mortar-bolt interface after shear failure (Fig. 9d).

To calibrate the smooth-joint normal stiffness, experimental deformability tests on smooth mortar-bolt interfaces were undertaken (based on the procedure used by Shang et al. [40]). The laboratory samples used in the normal deformability tests are the same as those shown in Fig. 9b. Identical samples without the mortar-bolt interface were also prepared and they were uniaxially compressed. Normal force and normal deformation of the mortar samples with and without the horizontal mortar-bolt interface were recorded during loading. Normal deformation of the mortar-bolt interface was estimated by subtracting the normal deformation of the mortar sample from the normal deformation of the sample with a mortar-bolt interface. Fig. 10 shows a representative testing result (the black line) where axial normal stress increased linearly against normal displacement. Then, numerical deformability tests were undertaken and smooth joint normal stiffness was calibrated by a trial-and-error process to match the inclination of the back line (Fig. 10). See [40] for a detailed description of the experimental and numerical deformability tests. The numerical result is compared with the laboratory test result, as shown in Fig. 10; and the corresponding calibrated micro-parameters are listed in Table 3.

5. Results and interpretation

5.1 Mortar-bolt interface debonding and subsequent mortar rupture

From the DEM simulation, it is observed that the mortar-bolt interface debonded progressively prior to the rupture of the surrounding cement mortar. Fig. 11 shows these two procedures quantitatively (rib angle β=90°and normal stress=4 MPa), where the measured and simulated stress-displacement curves (Figs. 11A and 11B) and key snapshots (Fig. 11C) are presented (**a**-**h**).

As shown in Fig. 11A, stresses within the mortar were measured at 25 different locations by the measurement spheres, as indicated in the inserted diagram. The monitored stress-displacement curves are shown in Fig. 11A. A resultant stress-displacement curve was obtained (the black line) and used for assessing the shear characteristics of the sample under direct shear. It can be seen that the resultant stress-displacement curve matched well with the experimental result (the black dotted line in Fig. 11A).

Fig. 11B shows a close-up view of the stress-displacement curves within the horizontal displacement of 0.5 mm, where the progressive debonding failure of the mortar-bolt interface was illustrated. The numerical test initiated at Point **a** (Figs. 11B and 11C), followed by the crack initiation around the bolt ribs (Point **b**); cracks propagated at Point **c** and coalesced at Point **d** where a peak stress of 1.21 MPa was measured (which is the bond strength of the mortar-bolt interface). The mortar-bolt interface debonded completely at Point **e** (Figs. 11B and 11C). Stress oscillations were observed after the appearance of the peak stress, which is related to the progressive failure/debonding of the mortar-bolt interface, especially at the rib areas leading to a direct interlocking between the ribs and the mortar.

The bolt ribs interacted with the adjacent cement mortar due to the mechanical interlocking before the mortar-bolt interface debonded completely (i.e., Point **e**). A large number of tensile and shear micro-cracks initiated around the ribs at Point **f**, which is related to the stress concentration due to interlocking. The shear strength of this sample was reached at Point **g** (6.2 MPa) and the cement mortar was completely ruptured, as shown by the diagram **g** in Fig. 11C. Shear stress was then reduced until the end of the test run (Point **h** in Figs. 11A and 11C). A macro-fracture with an inclination of around 52° was generated around a rib, while sub-horizontal macro-fractures were created around the other two ribs. Fig. 12 shows a detailed description of the mortar rupture process between Points **f** and **g** in Fig. 11. It can be seen that both tensile and shear micro-cracks were induced within the mortar due to the mortar-bolt interaction. After debonding of the mortar-bolt interface, cracks initiated around the three ribs but propagated with different speeds, which is related to the unequal stress distribution as unveiled by the stresses measured using the measurement spheres (Fig. 11A).

Fig. 13 shows the cumulative number of micro-cracks versus horizontal displacement (observed in Fig. 11). In the close-up view, the debonding point of the mortar-bolt interface is indicated at a horizontal displacement of 0.085 mm, where the numbers of both shear and tensile micro-cracks stopped increasing (Point **e** in Figs. 11B and 11C). After that, the numbers of tensile and shear micro-cracks increased dramatically due to the rupture of the mortar. Orientations of the micro-cracks generated at the interface debonding point (Point **e** in Fig. 11) and at the sample failure point (Point **g** in Fig. 11) are plotted in steronets (equal-area projection), as shown in Fig. 14. The micro-cracks (discs) are plotted as poles and are not show in the steronets for clarity. Contour lines represent the statistical pole concentration and contour interval is set to 1 for comparison and corresponding legends are indicated in each diagram. The filled contoured areas in Fig. 14a represented densities of 1-6% per 1% area for the micro-cracks, while the maximum density was increased to 8% per 1% area because more micro-cracks were generated due to the rupture of the mortar (Figs. 12 and 14b). It also can be seen that the orientations of the micro-cracks (poles to the crack discs) generated at the mortar-bolt interface debonding point concentrated at the centre of the steronet (Fig. 14a). The inclinations of these micro-cracks were less than 30°, which indicates that the orientations of the micro-cracks induced at the interface debonding point were largely controlled by the orientation of the mortar-bolt interface (which is sub-horizontal). The slight variation (0°-30°) in the crack orientations is associated with the spherical properties of the particles as well as the existence of the bolt ribs. This interpretation agrees well with the observation from Fig. 11 (at Point **e**). At the mortar rupture point (Point **g** in Fig. 11), a large number of micro-cracks with much higher inclinations (30°~ 90°) were created within the mortar (Fig. 14b), demonstrating some degrees of uncertainties. Interestingly, the orientations of the micro-cracks generated at this point distributed symmetrically in a broad sense, which can be related to the symmetrical nature of the rock bolt model established in the study.

5.2 Stress-displacement characteristics

Figs. 15-17 show the simulated (resultant) stress-displacement curves for cases with different rib angles and confining pressures; and corresponding experimental results are also included for comparison. Overall, the numerical results matched well with experimental measurements, although somewhat smaller shear strengths were measured in the simulations for the case β = 30° (Fig. 15a). The smaller strength measured using the DEM model for the 30° case is probably associated with the weak interlocking behaviour between the lower-inclined ribs and the mortar, which will be further discussed in the following section. Some stress oscillations of the DEM results were observed in the post-peak regions (Figs. 15a and 16a), which are related to the sudden splitting failure of the flat-jointed particles (due to the presence of the 3D flat interface).

Another main finding is that the progressive debonding processes of the mortar-bolt interfaces were revealed in the DEM simulations (Figs. 15b and 16b) and they often occurred within a horizontal displacement of 0.3 mm. However this phenomenon is extremely difficult to be observed in the laboratory experiments.

5.3 Rupture patterns of the cement mortar

The rupture patterns of the mortar observed in the DEM simulations and experiments (rib angle β = 30°) are shown in Fig. 18. The yellow dashed lines represent the primary macro-fractures. The 3D micro-crack distributions are presented without showing particles for a clear visualisation (Figs. 18c and 18d). The red and blue discs represent shear and tensile micro-cracks, respectively. As shown in Fig. 18a, a clear slip was observed between the low inclined ribs and the mortar (after the shear failure of the interface), forming a height difference (around 1.3 mm) between the ribs and the mortar. The slip behaviour is related to the weak interlocking at the interface of the mortar and the low inclined bolt ribs.

A macro-fracture with an inclination of around 82° was induced at one of the ribs, accompanied by some sub-horizontal fractures due to the mortar-bolt interactions (Figs 18a and 18c). Similar phenomena were observed in the laboratory experiments under the same boundary condition (normal stress=2 MPa, Fig. 18e). A macro-fracture with an inclination of 71° was induced (Fig. 18e), which was smaller than that observed in the DEM simulation (82°, Fig. 18a). Likewise, a slip was also observed at the rib-mortar interface and a height difference of 1.5 mm was created (see the close-up view, Fig. 18e).

When the confining pressure was increased to 4 MPa (Figs. 18b), the slip and shear phenomena still existed and a macro-fracture with an inclination of 77° was generated (Figs. 18a and 18b). Fig. 18d shows that more micro-cracks were generated in comparison with the case under a lower confining pressure (2 MPa). It is observed that the slip-induced height differences between the bolt ribs and the mortar were 1.1 mm in the DEM simulation and 1.0 mm in the laboratory experiment. They were smaller than the corresponding cases under a higher confining pressure (i.e., 4 MPa).

Figs. 19 and 20 show the mortar rupture patterns for cases of higher rib angles (i.e., 60° and 90°). In general, the simulation results are in close agreement with the laboratory test results. Interestingly, the slip behaviour (observed in Fig. 18) vanished for both laboratory tests and numerical simulations (see the close-up views in Figs. 19f and 20e, the height difference between the ribs and the mortar is neglectable). This can be attributed to the much higher interlocking effect due to the high inclined ribs.

Besides the inclined macro-fractures, some sub-horizontal fractures were induced, especially for the cases under a relatively higher confining pressure (i.e. 4 MPa, Figs. 19b and 20b). These observations indicate that the parallel-shear failure dominated when rib angles were 60° and 90°. It should be noted that there are some discrepancies in pattern between the sub-horizontal fractures created in the DEM simulations and Laboratory experiments. This discrepancy however cannot be explained so far. It is suggested that further research needs to be conducted to clarify this observation.

6. Discussion, limitations and future research priorities

6.1 Mortars with different particle size distributions

In the study, the cement mortar was discretised and represented as spherical particles that were bonded at their contacts without considering its real micro-structure [48, 49], which of course is a simplification of real mortars. This simplification practice however has been widely used in particulate simulations for representing various materials [27–29,31].

It has been reported that the particle size is an intrinsic parameter that affects mechanical properties of a solid material [33,35]. Simulation results of this study are based on a specific particle size distribution (Table 2) which is determined in the calibration process (Section 4). To verify the reliability of the reported results (Section 6) and further understand the effect of particle size on simulation results, three additional DEM simulations with different average particle radii, $D_{avg.}$, (Cases A, C and D in Fig.21) were performed following the method used by Potyondy and Cundall [35]. The numbers of the particles forming the mortars of Cases A-D are 98870, 29346, 6325, 3652, respectively. All other micro-properties remained constant, as shown in Tables 2 and 3. The DEM model setup and bolt profile were the same as that described in Section 3. Simulations were conducted under a constant normal stress of 4 MPa. Fig. 21 shows a comparison of the failure patterns observed after the simulations; the previously reported result (i.e., Case B) is included for comparison. It can be seen that parallel-shear failures (along the mortar-bolt interfaces) dominated for all cases except the Case D, for which the average particle size was the largest among the simulated cases ($D_{avg.}$=1.5 mm), leading to a dramatic decrease in the number of particles and therefore a different failure pattern.

Fig. 22 shows that shear strength increased with the increase of the average particle size. The increases in shear strength for Cases C and D were due to the dramatic decreases in the number of particles (6325 and 3652) in comparison with Cases A and B (98870 and 29346). The smaller number of particles might not sufficient to simulate the failure mechanisms for this particular study. Notably, the shear strengths measured in Cases A and B (6.1 and 6.15 MPa) were close to the laboratory measurement (6.2 MPa), as shown in Fig. 22; and the reported result in Section 5 (Case B) shows a better closeness to the laboratory measurement.

The current numerical investigation is based on the SRBM proposed by Yokota et al. [33]. This simplified model allows the investigation of the mechanical and deformable behaviours of the mortar-bolt interface on the assumption that the bond strength of mortar-rock interface is much stronger than that of mortar-bolt interface. This assumption implies that failure will dominantly occur at the mortar-bolt interface rather than the mortar-rock interface, although the way of failure sometimes depends on the roughness of bolt and the type of cement mortars [50]. Besides, the possible chemical effect (i.e., erosion) of the cement composition on the micro-structure of the steel bolt surface is ignored for simplification [51]. Additionally, the elongation and twisting of the rebar bolt in the experiment are assumed insignificant. Practically, these assumptions are acceptable for simple stress conditions (without creeping and dynamic ejection), as pointed out by Li [9] and Siger [52]. Technically, the aforementioned assumptions are testable and allow the SRBM to be tested in the laboratory. In future research, the mortar-bolt interface behaviour of a full section of a fully grouted rebar bolt (Fig. 2a) is suggested to be investigated by numerical simulations and results can be compared with those reported in the current study (based on the SRBM).

6.2 Effect of the bolt profile configuration

Literature confirms that rib spacing (R_s) and rib height (R_h) of a rebar bolt are most important profile parameters determining the load transfer capacity for a fully grouted rebar bolt subjected to external load. These two parameters mainly affect the mechanical interlocking between bolt ribs and adjacent mortars. In this study, for validation purpose, a constant rib spacing (17.8 mm) and rib height (2 mm) were used in DEM simulations (Fig. 6b), which are the same as those values used in the laboratory experiment (Fig. 3). Simulated results are in broad agreements with experimental observations in terms of peak shear strength (Figs. 15-17) and failure patterns (Figs. 18-20). To examine the effects of rib spacing and rib height on the simulation results, two series of DEM simulations were additionally performed, considering the representative rib spacing and rib height values of the rebar bolts widely used in mining industries in China and Australia [53].

6.2.1 Rebar bolts with different rib spacings

For the first series of simulations, rib spacings were varied between 12.5 mm and 50 mm, as illustrated in Fig. 23. All other parameters were fixed (as shown in Tables 2 and 3) and the numerical setups are the same as that described in Fig. 6. Fig. 23 shows a comparison of the failure patterns of the simulated cases (I-IV). It can be seen that parallel-shear failure dominated for all cases. All mortars in neighbouring ribs were sheared except the Case V, where a much higher rib spacing was adopted (50 mm), leading to a different failure pattern.

Fig. 24 shows the relationship between shear strength and rib spacing (R_s). It can be seen that the variation in shear strength between specimens with different rib spacings was not large (within 14%). The highest shear strength of 6.3 MPa was measured when the rib spacing was 25 mm (Fig. 24). It dropped to 5.54 MPa when rib spacing was reduced to 12.5 mm and the decrease in shear strength was also observed when rib spacing was increased (for example, 5.39 MPa at R_s=50 mm, Fig. 24). The shear strength increased slightly with the increasing of rib spacing and then decreased at a particular rib spacing (22.7 mm, Fig. 24); this observation is similar to previous studies [53, 54], although in their studies the peak load appeared at a rib spacing of 37.5 mm. This discrepancy is related to the differences in the strength of the mortars and in other rib profile parameters (such as the rib height and rib angle). It is therefore suggested that the optimum rock bolt spacing should be assessed and selected case by case, based on the rib profile and mortar strength.

6.2.2 Rebar bolts with different rib heights

The second series of simulations involved additional three cases having a rib height of 1.0, 1.5 and 2.5 mm, respectively (Cases 1, 2 and 4 in Fig. 25). The rib spacing was kept constant at 17.8 mm and other setup parameters remained the same as those shown in Fig. 6. A comparison of failure patterns is shown in Fig. 25. It can be seen that the width of the rupture zones increased and became much wider when the rib height was increased. The difference was also demonstrated by the variation in the shear strength, as illustrated in Fig. 26. It can be seen that shear strength increased when the rib height was increased (Fig. 26). This finding revealed that there is a significant influence of rib height on the rockbolting capacity (based on the reported rib profile configuration).

6.3 Boundary condition

It is accepted that boundary conditions affect shear characteristics [40]. In this study, all laboratory experiments and numerical simulations were performed under constant normal load (CNL) boundary conditions. The effect of constant normal stiffness (CNS) boundary condition, which also exists in nature, especially in the underground engineering applications, is ignored. It is well known that setup of a CNS shear test is extremely difficult and it is rare to see the laboratory CNS shear tests in literature. Considering the difficulty of the experimentation, it is therefore suggested that the mortar-bolt interface behaviour under CNS boundary condition can be studied using the numerical model proposed by Shang et al. [40].

7. Summary and conclusions

The primary aim of this paper is to investigate the micro-macro failure mechanisms underlying the shear failure of fully grouted rebar bolts that often observed in civil and mining engineering applications. A three-dimensional DEM model was established based on a simplified rock bolt model. The DEM model was calibrated and verified against a series of laboratory experiments including uniaxial compression and triaxial tests on cement mortars, and direct shear and normal deformability tests on planar mortar-bolt interfaces.

The established DEM model was used to study the mortar bolt interactions under direct shear; and the simulation results were validated against laboratory experiments and a broad agreement was observed. The following conclusions can be drawn:

(1) The DEM investigation in this study has led to two main observations at micro- and macro- scale levels. The first is that the mortar-bolt interface often debonded progressively at a small horizontal displacement (up to 0.3 mm in this study). The progressive debonding process was represented by the initiation, propagation and coalescence of the micro-cracks on the mortar-bolt interface, which are not achievable and observable through current experimentation. The second main observation is on the mortar rupture. It occurred just after the debonding of the mortar-bolt interface, which is due to the mechanical interlocking between the bolt ribs and the cement mortar.

(2) The DEM results presented in the study exhibited a better predication of the mortar-bolt interface behaviour with respect to shear strength and failure patterns when the rib angles were relatively high (i.e., 60° and 90° in the study). A somewhat smaller shear strength however was measured in the DEM simulations than that from the laboratory experiments when the rib angle was 30°.

(3) A slip failure was observed in the simulations when rib angle was relatively small (β=30° in the study). While the slip phenomenon vanished when the rib angles were increased up to 60° and 90°; and the parallel shear rupture dominated, forming some sub-horizontal macro-fractures.

(4) The number of micro-cracks within the mortar increased significantly when the confining pressure and rib angles were increased, leading to a much higher level of mechanical interlocking.

(5) The mortar-bolt model simulated in this study often failed within a horizontal shear displacement of 2 mm. It is also observed that, for a specific rebar bolt, a high inclined macro-crack was induced at the location close to one of the bolt ribs. The inclinations of the macro-cracks varied with the rib angles and confining pressures, but all greater than 50° relative to the mortar-bolt interface (sub-horizontal).

(6) The effect of rib angle on the shear strength was relatively small, in comparison with that from rib spacing and rib height. For this particular study, the highest shear strength of approximately 6.4 MPa was measured at a rib spacing of 22.7 mm. It is therefore suggested that rib spacing and rib height should be carefully assessed for the bolt profile optimisation and a slightly higher rib spacing and rib height may result in a higher rockbolting capacity, however a balance between efficiency and cost needs to be made by manufacturers.

Acknowledgement

The laboratory experiments reported in the study were performed at the Kajima Corporation, Japan.

References

[1] S. Ma, N. Aziz, J. Nemcik, A. Mirzaghorbanali, The effects of installation procedure on bond characteristics of fully grouted rock bolts, Geotech. Test. J. 40(5) (2017), 846-857.

[2] C. Cao, T. Ren, C. Cook, Y. Cao, Analytical approach in optimising selection of rebar bolts in preventing rock bolting failure, Int. J. Rock. Mech. Min. Sci. 72 (2014), 16–25.

[3] W. Nie, Z.Y. Zhao, Y.H. Ning, W. Guo, Numerical studies on rock bolts mechanism using 2D discontinuous deformation analysis, Tunn. Undergr. Space Technol. 41 (2014), 223-233.

[4] E. Hoek, D.F. Wood, Support in underground hard rock mines, Underground Support Systems 35 (1987), 1–6.

[5] A.J. Hyett, W.F. Bawden, R.D. Reichert, The effect of rock mass confinement on the bond strength of fully grouted cable bolts, Int. J. Rock Mech. Min. Sci. Geomech. Abstr. 29(5) (1992), 503–524.

[6] P.K. Kaiser, S. Yazici, J. Nose, Effect of stress change on the bond strength of fully grouted cables, Int. J. Rock Mech. Min. Sci. & Geomech. Abstr. 29(3) (1992), 293–306.

[7] G. Rong, H.C. Zhu, C.B. Zhou, Testing study on working mechanism of fully grouted bolts of thread steel and smooth steel, Chin. J. Rock Mech. Eng. 23(3) (2004), 469-475.

[8] N.I. Aziz, H. Jalalifar, J. Concalves, Bolt surface configurations and load transfer mechanism, In: Proceedings of the 7th Underground Coal Operators Conference, Wollongong (2006) 236–244.

[9] C. Li, Field observations of rock bolts in high stress rock masses, Rock Mech. Rock Eng. 43 (2010), 491–496.

[10] K. Sugawara, A. Sato, Y. Obara, H. Shimada, Crack opening analysis using the X-rays CT data, Proc. of the 9th Congress of ISRM 2 (1999), 1019-1022.

[11] S. Yazici, P.K. Kaiser, Bond strength of grouted cable bolts, Int. J. Rock Mech. Min. Sci. & Geomech. Abstr. 29(3) (1992), 279-292.

[12] B. Benmokrane, A. Chennouf, H.S. Mitri, Laboratory evaluation of cement-based grouts and grouted rock anchors, Int. J. Rock Mech. Min. Sci. & Geomech. Abstr. 32 (1995), 633–642.

[13] C. Li, B. Stillborg, Analytical models for rock bolts, Int. J. Rock Mech. Min. Sci. 36 (1999), 1013–1029.

[14] F.F. Ren, Z.J. Yang, J.F. Chen, W.W. Chen, An analytical analysis of the full-range behaviour of grouted rockbolts based on a tri-linear bond-slip model, Constr. Build. Mater. 24 (2010), 361-370.

[15] S. Ma, J. Nemcik, N. Aziz, An analytical model of fully grouted rock bolts subjected to tensile load, Constr. Build. Mater. 49 (2013), 519-526.

[16] D. Bernaud, P.D. Buhan, S. Maghous, Numerical simulation of the convergence of a bolt-supported tunnel through a homogenization method, Int. J. Numer. Anal. Method. 19(4) (1995), 267–288.

[17] L. He, X.M. An, X.B. Zhao, Z.Y. Zhao, J. Zhao, Development of a unified rock bolt model in discontinuous deformation analysis, Rock Mech. Rock Eng. (2017), https://doi.org/10.1007/s00603-017-1341-9.

[18] D. Deb, K.C. Das, Modelling of fully grouted rock bolt based on enriched finite element method, Int. J. Rock Mech. Min. Sci. 48 (2011), 283–293.

[19] J. Nemick, S. Ma, N. Aziz, T. Ren, X. Geng, Numerical modelling of failure propagation in fully grouted rock bolts subjected tensile load, Int. J. Rock Mech. Min. Sci. 71 (2014), 293-300.

[20] M. Moosavi, R. Grayeli, A model for cable bolt-rock mass interaction: integration with discontinuous deformation analysis (DDA) algorithm, Int. J. Rock Mech. Min. Sci. 43(4) (2006), 661-670.

[21] W. Nie, Z.Y. Zhao, Y.J. Ning, J.P. Sun, Development of rock bolt elements in two-dimensional discontinuous deformation analysis, Rock Mech. Rock Eng. 47 (2014), 2157-2170.

[22] Y. Li, H. Zhou, L. Zhang, W. Zhu, S. Li, J. Liu, Experimental and numerical investigations on mechanical property and reinforcement effect of bolted jointed rock mass, Constr. Build. Mater.126 (2016), 843–856.

[23] X. Li, Finite element modelling of skewed reinforced concrete bridges and the bond-slip relationship between concrete and reinforcement, Master thesis, Auburn University, (2007), pp.162.

[24] G. Wang, Y. Zhang, Y. Jiang, S. Wang, W. Jing, Macro-micro failure mechanisms and damage modelling of a bolted rock joint, Adv. Mater. Sci. Eng. (2017), https://doi.org/10.1155/2017/1627103.

[25] Z. Ge, Y.Y. Wang, Y. Hou, W.J. Sun, R.J. Sun, Evaluation of fracture in mortar subject to tension loading using phase field model and three point bending test, Mater. Des. 86 (2015), 121–128.

[26] Itasca Consulting Group Inc (2008) PFC3D manual, version 4.0. Minneapolis, Minnesota

[27] J. Shang, K. Duan, Y. Gui, K. Handley, Z. Zhao, Numerical investigation of the direct tensile behaviour of laminated and transversely isotropic rocks containing incipient bedding planes with different strengths, Comput. Geotech. (2017), https://doi.org/10.1016/j.compgeo.2017.11.007.

[28] T. Wang, W. Zhou, J. Chen, X. Xiao, Y. Li, X. Zhao, Simulation of hydraulic fracturing using particle flow method and application in a coal mine, Int. J. Coal Geol. 121(1) (2014), 1-13.

[29] J. Pan, Y. Feng, F. Jin, Y. Xu, Q. Sun, C. Zhang, D.R.J. Owen, Meso-scale particle modelling of concrete deterioration caused by alkali-aggregate reaction, Int. J. Numer. Anal. Meth. Geomech. 37 (2013), 2690-2705.

[30] H. Haeri, V. Sarfarazi, Numerical simulation of tensile failure of concrete using particle flow code (PFC), Comput. Concrete. 18(1) (2016), 39-51.

[31] Y.S. Jeong, S. Jeon, D.S. Cheon, Numerical study for mechanical behaviour of cement mortar using 3D particle flow code, Proc. Antumn Korea Society of Rock Mechanics (2005), 157–162.

[32] C. Lee, D. Lee, S. Jeon, The influence of excavation damaged zone on the mechanical and thermal behaviour of cement mortar block around an opening, KSCE J. Civ. Eng. 17(6) (2013), 1263–1274.

[33] Y. Yokota, Z. Zhao, W. Nie, K. Date, K. Iwano, Y. Okada, Small scale behaviour along the boundary between the rock and bond material, Eurock 2018 – the ISRM European Rock Mechanics Symposium, accepted (2018).

[34] S.R. Hencher, L.R. Richards, Assessing the shear strength of rock discontinuities at laboratory and field scales, Rock Mech. Rock Eng. 48 (2015), 883–905.

[35] D.O. Potyondy, P.A. Cundall, A bonded-particle model for rock, Int. J. Rock Mech. Min. Sci. 41(8) (2004), 1329-1364.

[36] S. Wu, X. Xu, A study of the intrinsic problems of the classic discrete element method using flat-joint model, Rock Mech. Rock Eng. 49 (2016), 1813-1830.

[37] J.A. Vallejos, J.M. Salinas, A. Delonca, D.M. Ivars, Calibration and verification of two bonded-particle models for simulation of intact rock behaviour, Int. J. Geomech. (2017), https://doi.org/10.1061/(ASCE)GM.1943-5622.0000773.

[38] J. Zhou, L. Zhang, Investigation of the quasi-brittle failure of Alashan granite viewed from laboratory experiments and grain-based discrete element modelling, Materials (2017), doi: 10.3390/ma10070835.

[39] D. Huang, J. Wang, S. Liu, A compressive study on the smooth joint model in the DEM simulation of jointed rock masses, Granul. Matter 17 (2015), 775–791.

[40] J. Shang, Z. Zhao, S. Ma, On the shear failure of incipient rock discontinuities under CNL and CNS boundary conditions: Insights from DEM modelling, Eng. Geol. 234 (2018), 153-166.

[41] D.O. Potyondy, PFC 3D flat joint contact model version 1, Itasca Consulting Group (2013). [42] Itasca Consulting Group Inc., PFC3D manual, version 4.0. Minneapolis. Minnesota (2008).

[43] J. Shang, S.R. Hencher, L.J. West, Tensile strength of incipient rock discontinuities, In: Proceedings of the ISRM regional symposium Eurock 2015 & 64th Geomechanics Colloquium, Salzburg, Austria, (2015) pp 565–570.

[44] J. Shang, S.R. Hencher, L.J. West, Tensile strength of geological discontinuities including incipient bedding, rock joints and mineral veins, Rock Mech. Rock Eng. 49(11) (2016), 4213-4225.

[45] J. Shang, S.R. Hencher, L.J. West, Z. Zhao, Tensile strength of large-scale incipient rock joints: a laboratory investigation, Acta Geotech. (2018b), https://doi.org/10.1007/s11440-017-0620-7.

[46] ASTM standard C496, Standard tests method for splitting tensile strength of cylindrical concrete specimens, (1996), West Conshohocken, United States.

[47] ASTM standard 192, Standard practice for making and curing concrete test specimens in the laboratory, (2002), West Conshohocken, United States.

[48] M. Arandigoyen, J.I. Alvarez, Pore structure and mechanical properties of cement-lime mortars, Cem. Concr. Res. 37(5) (2007), 767-775.

[49] S. Das, A. Kizilkanat, N. Neithalath, Crack propagation and strain localization in metallic particulate-reinforced cementitious mortars, Mater. Des. 79 (2015), 15–25.

[50] G.A. Rao, B.H.R. Prasad, Influence of the roughness of aggregate surface on the interface bond strength, Cem. Concr. Res. 32 (2002), 253-257.

[51] M.N.A. Khalaf, Steel/mortar interfaces: Microstructural features and mode of failure, Cem. Concr. Res. 9 (1979), 197–208.

[52] S.P. Singer, Field verification of load transfer mechanics of fully grouted roof bolts, US Bureau of Mines: reports of investigations 9301 (1990), pp.18.

[53] C. Cao, Bolt profile configuration and load transfer capacity optimisation. University of Wollongong, Australia, PhD thesis (2012), pp 272.

[54] N.I. Aziz, H. Jalalifar, J. Concalves, Bolt surface configurations and load transfer mechanism. In: Proceedings of the 7th Underground Coal Operators Conference, Wollongong, 5-7 July (2016), 236-44.

[55] N. Cho, C.D. Matrin, D.C. Sego, A clumped particle model for rock, Int. J. Rock Mech. Min. Sci. 44(7) (2007), 997-1010.

Figure captions

Fig. 1. Debonding failure of a mortar-bolt interface subjected to axial loading. Adapted from [15].

Fig. 2. a Schematic diagram of a fully grouted rebar bolt and **b** the simplified rock bolt model (not to scale).

Fig. 3. Representative laboratory samples with three different rib angles (**a** β=30°, **b** β=60°, **c** β=90°).

Fig. 4. Schematic diagram of the experimental setup (shear box model: PHI-10; figure not to scale).

Fig. 5. Contact models used in the study. **a** Linear Parallel Bond Contact Model (after [55]); **b** Flat Joint Contact Model (adapted from [41]); **c** Smooth Joint Contact Model; and **d** Linear Model.

Fig. 6. **a** Setup of the DEM model of the direct shear test; **b** A close-up view of the mortar-bolt interface; and **c** An example of the contacts between particles; the four differnet contact models are shown as cylinders with different colours, and particles and walls are not show for clarity.

Fig. 7. Calibration of the flat joint contact model. **a** Comparison of the stress-strain curves from laboratory experiments and DEM simulation; **b** Failure patterns of the laboratory samples (S1-S6) after uniaxial compression; and **c** Failure pattern of a DEM sample under the same loading condition.

Fig. 8. Comparison of the experiemental results and numerical results of triaxial compression tests.

Fig. 9. Comparison of the direct shear test results from the laboratory experiement and DEM simulation (under a normal stress of 2 MPa). **a** Shear stress versus horizontal displacement; **b** and **c** Post-failures of the laboratory experiment and the DEM simulation, respectively; and **d** Micro-cracks induced on the mortar-bolt interface after shear failure**.**

Fig. 10. Axial stress against normal displacement measured in the normal deformability tests: comparison of laboratory test and DEM simulaiton.

Fig. 11. Progressive debonding of the mortar-bolt interface and shear ruputre of the mortar subjected to shearing. **A** Stress-displacement curves measured in the simulation using the 25 measuremet spheres (MS, shown in the insert diagram); the black line represents the resultant stress-displacement and it was compared with that mesured from the laboratory experiment (back dotted line); **B** A close-up view showing the initial stage of the simulaiton (at a horizontal displacement of 0.5 mm); **C** Frames captured at key stages (maked as **a**-**h** in **A** and **B**) in the simulation, in which the progessive debonding of the mortar-bolt interface and ruputre failure of the mortar are presented (β=90°, R_s=17.8 mm, R_h=2 mm and applied normal stress=4 MPa). For more details, see text.

Fig. 12. Mortar rupture due to mechanical interlocking (Frames were captured between Points **f** and **g**, as shown in Fig. 11).

Fig. 13. Number of micro-cracks (shown in the Frame **h** in Fig. 11) against horizontal displacement.

Fig. 14. Contoured plots of the orientations of the induced micro-cracks monitored at the mortar-bolt interface debonding point (point **e** in Fig. 11) (**a**) and at the mortar rupture point (point **g** in Fig. 11) (**b**).

Fig. 15. Stress against horizontal displacement: a comparison between numerical simulations and experiemntal results (β=30° and normal stress=2 and 4 MPa). **a** Overall results and **b** a close-up view.

Fig. 16. Stress versus horizontal displacement: a comparison between numerical simulations and experiemntal results (β=60° and normal stress=2 and 4 MPa). **a** Overall results and **b** a close-up view.

Fig. 17. Stress against horizontal displacement: a comparison between numerical simulations and experiemntal result (β=90° and normal stress=2 MPa).

Fig. 18. Shear ruputre of the mortar observed in the DEM simulations with relatively low rib angles (β = 30°). **a** and **c** Normal stress=2 MPa; **b** and **d** Normal stress=4 MPa. Corresponding failure patterns observed in the laboratory experiments are included for comparison (**e** and **f**).

Fig. 19. Shear ruputre of the mortar observed in the DEM simulations for the cases with a rib angle β = 60°. **a** and **c** Normal stress=2 MPa; **b** and **d** Normal stress=4 MPa. Corresponding failure patterns observed in the laboratory experiments are included for comparison (**e** and **f**).

Fig. 20. Shear ruputre of the mortar observed in the DEM simulations for the cases with a rib angle β = 90°. **a** and **c** Normal stress=2 MPa; **b** and **d** Normal stress=4 MPa. Corresponding failure patterns observed in the laboratory experiments are included for comparisons (**e** and **f**).

Fig. 21. Shear failure of mortar-bolt interfaces with different particle size distributions.

Fig. 22. Shear strength of the mortars (shown in Fig. 21) versus average particle radius.

Fig. 23. Shear failure of mortar-bolt interfaces with different rib spacings

Fig. 24. Shear strength of the mortars (shown in Fig. 23) versus rib spacing

Fig. 25. Shear failure of mortar-bolt interfaces with different rib heights

Fig. 26. Shear strength of the mortars (shown in Fig. 25) versus rib height

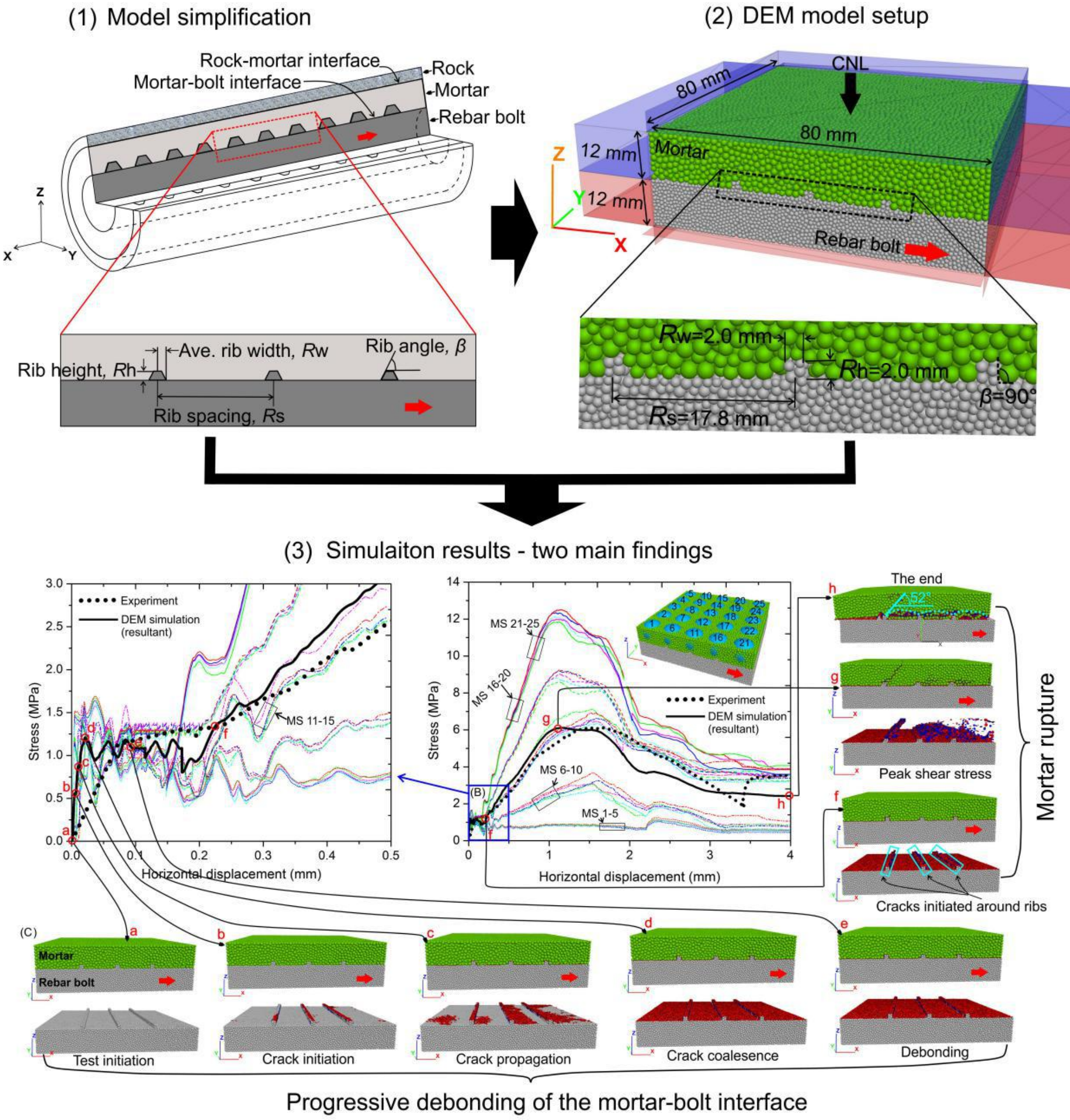

Graphical abstract

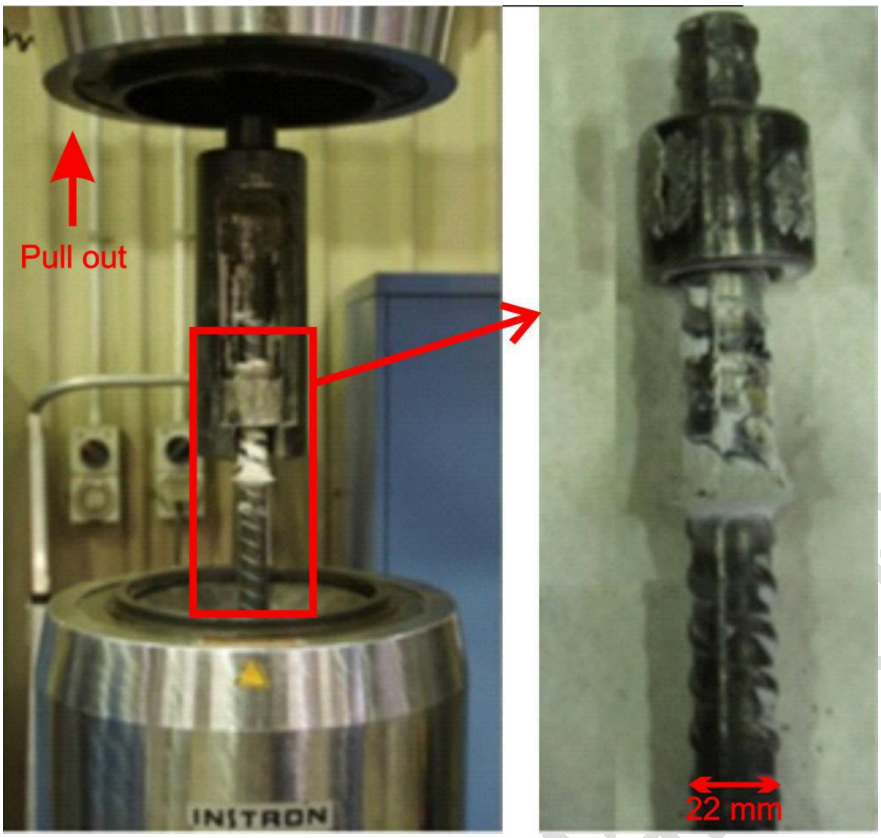

Fig 1

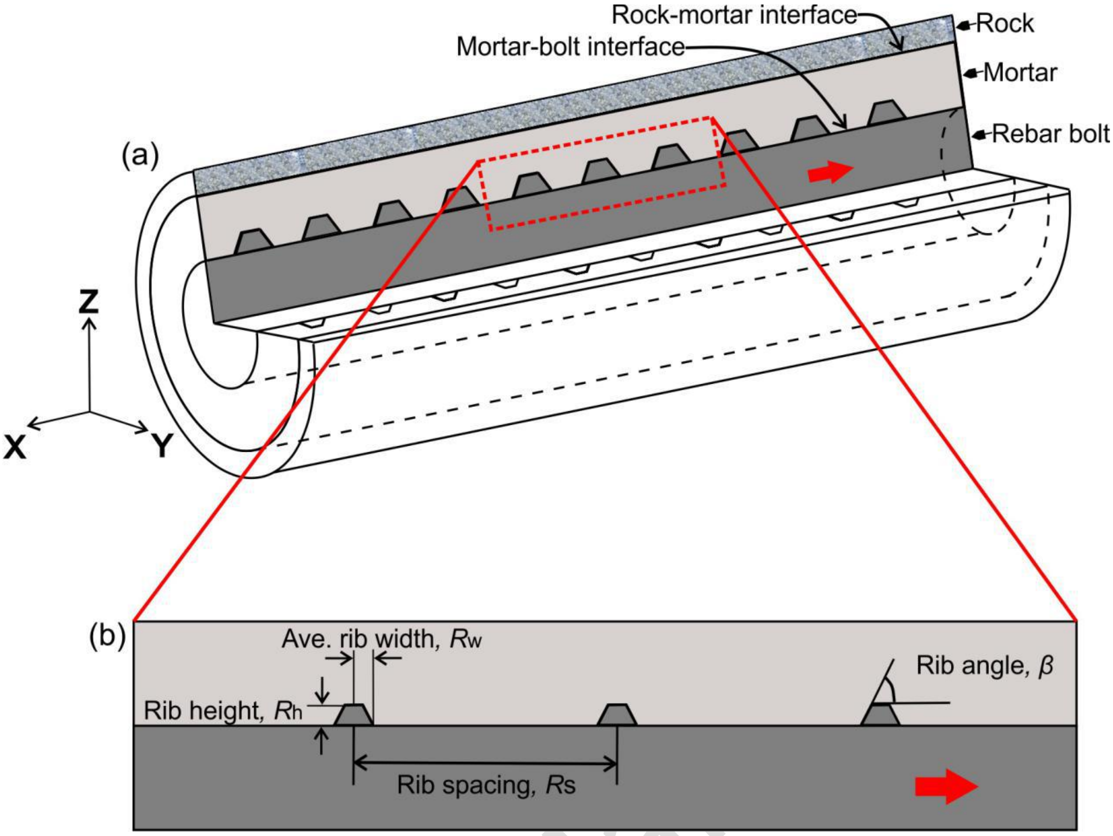
Rock-mortar interface
Mortar-bolt interface
Rock
Mortar
Rebar bolt
(a)
Z
X
Y
(b)
Ave. rib width, Rw
Rib height, Rh
Rib angle, β
Rib spacing, Rs

Fig 2

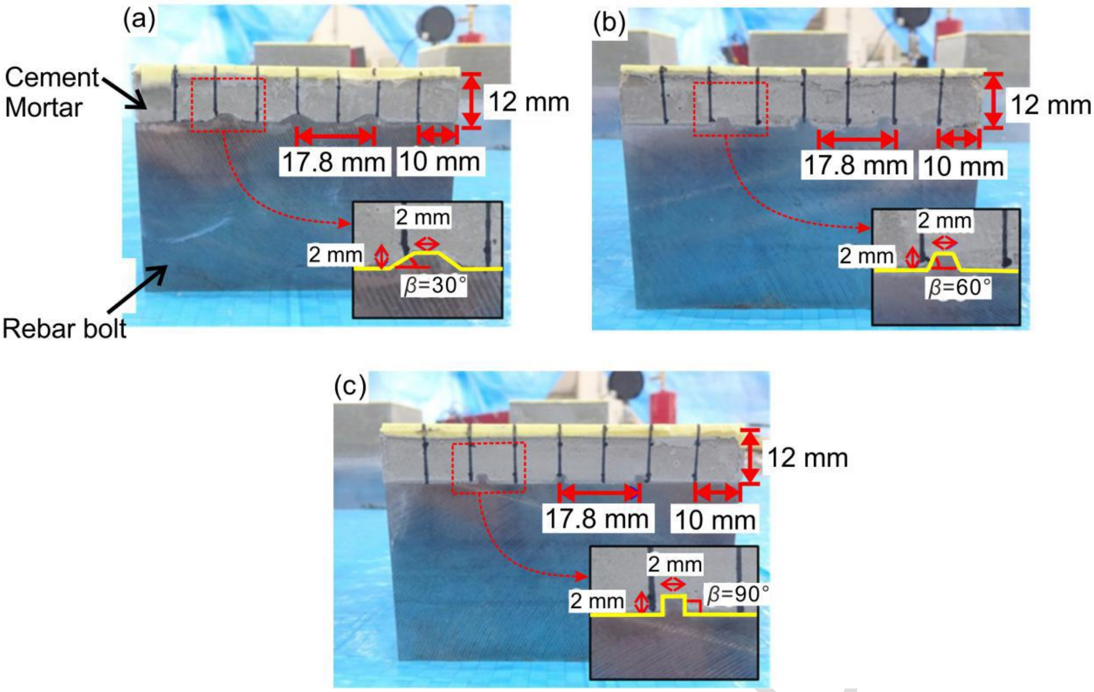
(a)
Cement
Mortar
12 mm
17.8 mm
10 mm
2 mm
2 mm
β=30°
Rebar bolt
(b)
12 mm
17.8 mm
10 mm
2 mm
2 mm
β=60°
(c)
12 mm
17.8 mm
10 mm
2 mm
2 mm
β=90°

Fig 3

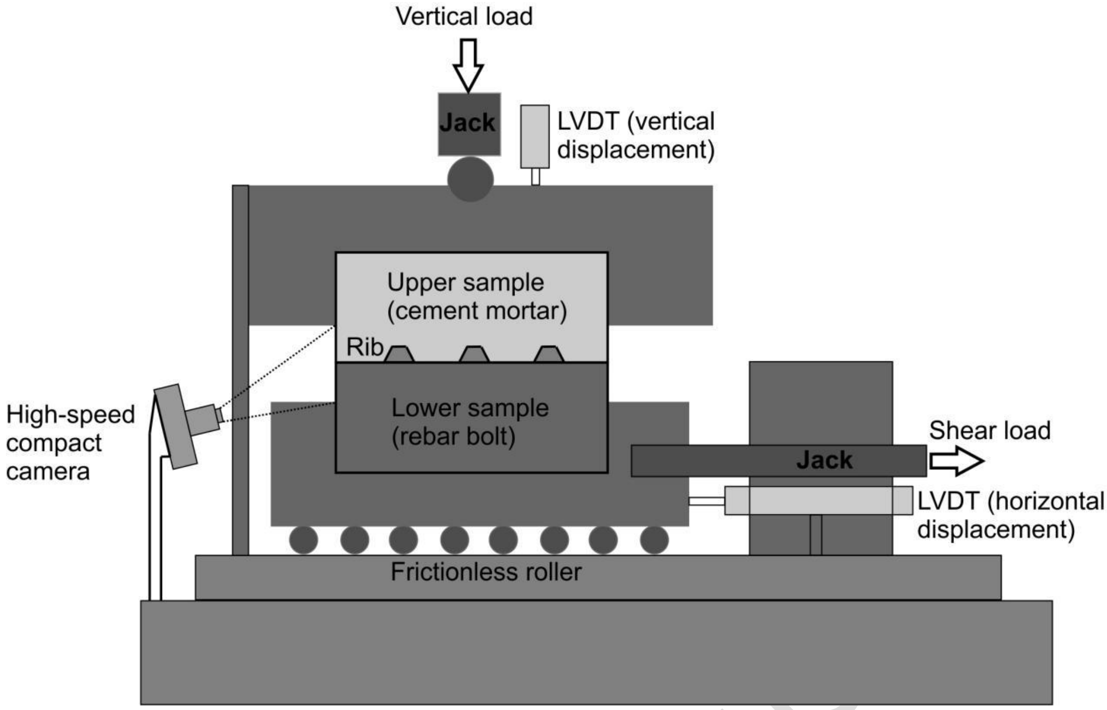
Vertical load
Jack
LVDT (vertical displacement)
Upper sample (cement mortar)
Rib
Lower sample (rebar bolt)
High-speed compact camera
Shear load
Jack
LVDT (horizontal displacement)
Frictionless roller

Fig 4

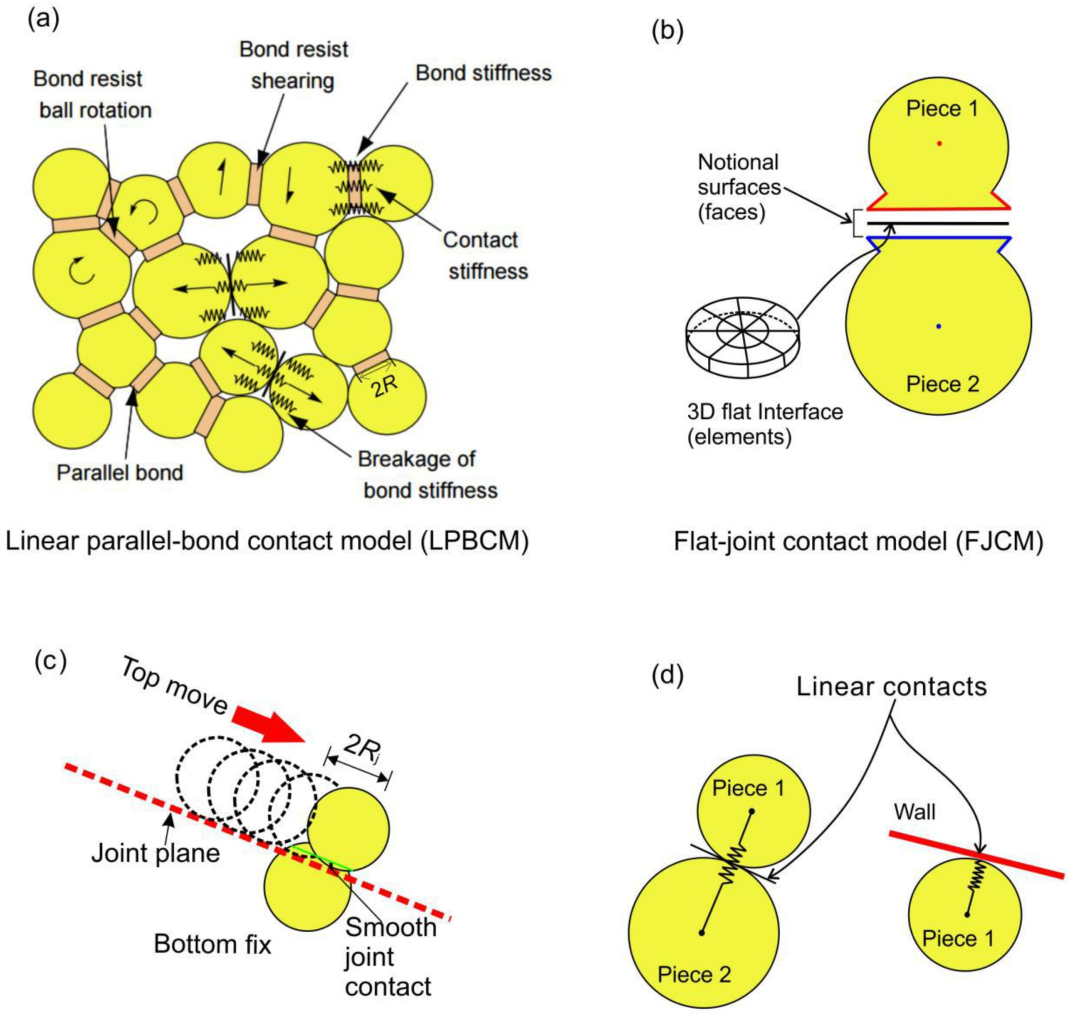

Linear parallel-bond contact model (LPBCM)

Flat-joint contact model (FJCM)

Smooth-joint contact model (SJCM)

Linear model (LM)

Fig 5

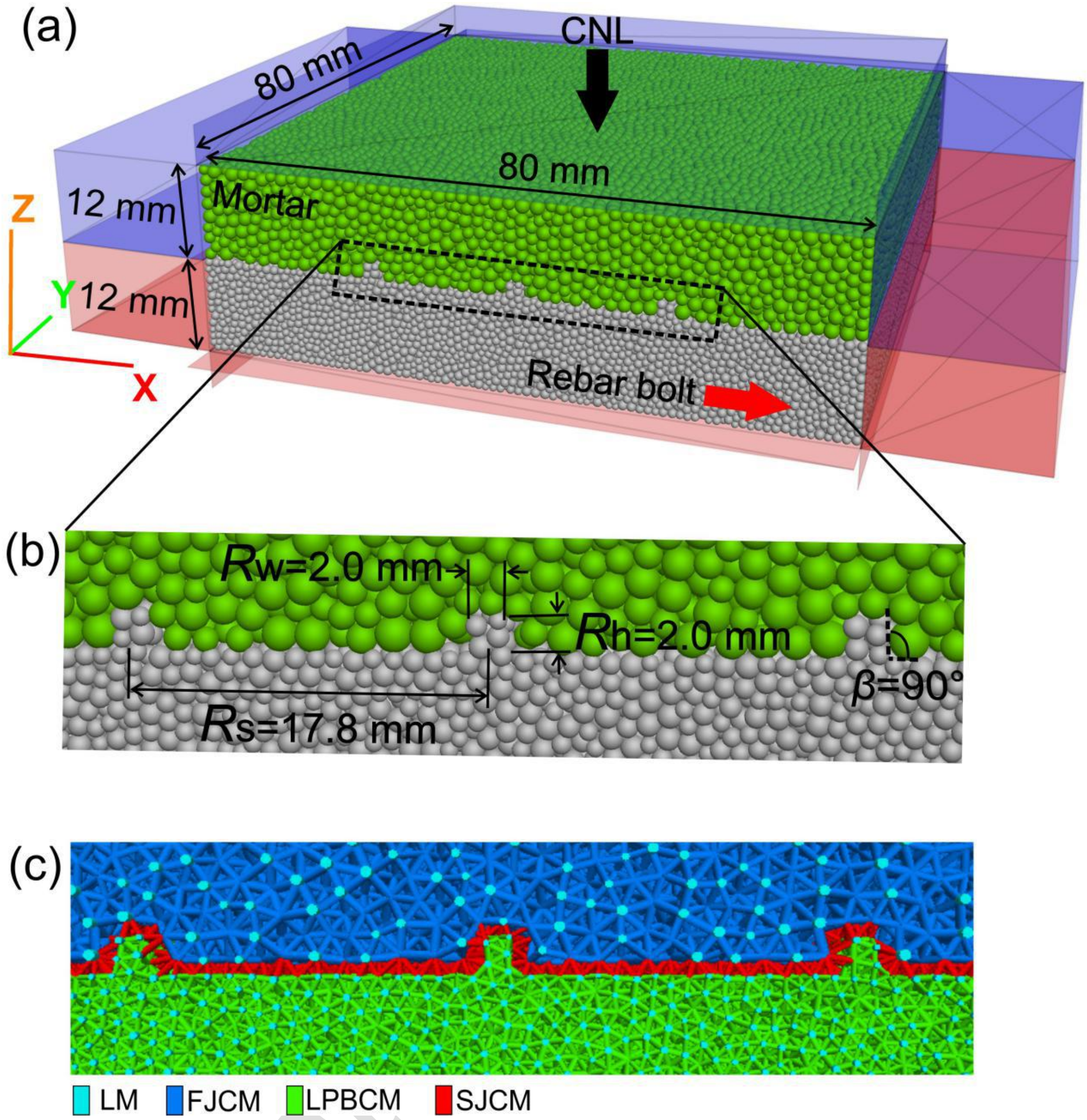

953

954 **Fig 4**

955

956

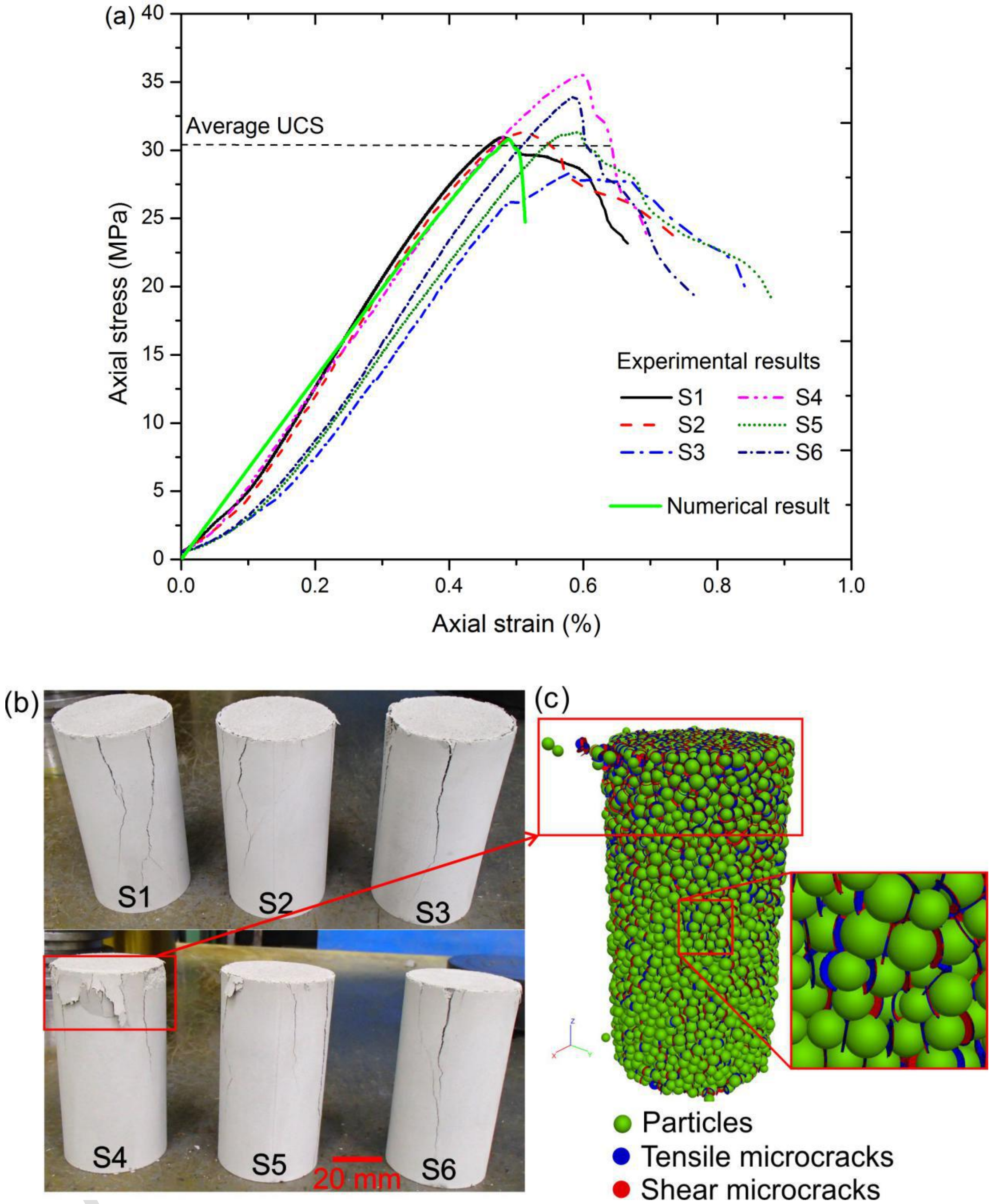
(a)
Average UCS
Axial stress (MPa)
Axial strain (%)
Experimental results
S1
S2
S3
S4
S5
S6
Numerical result
(b)
S1
S2
S3
S4
S5
S6
20 mm
(c)
Particles
Tensile microcracks
Shear microcracks

Fig 7

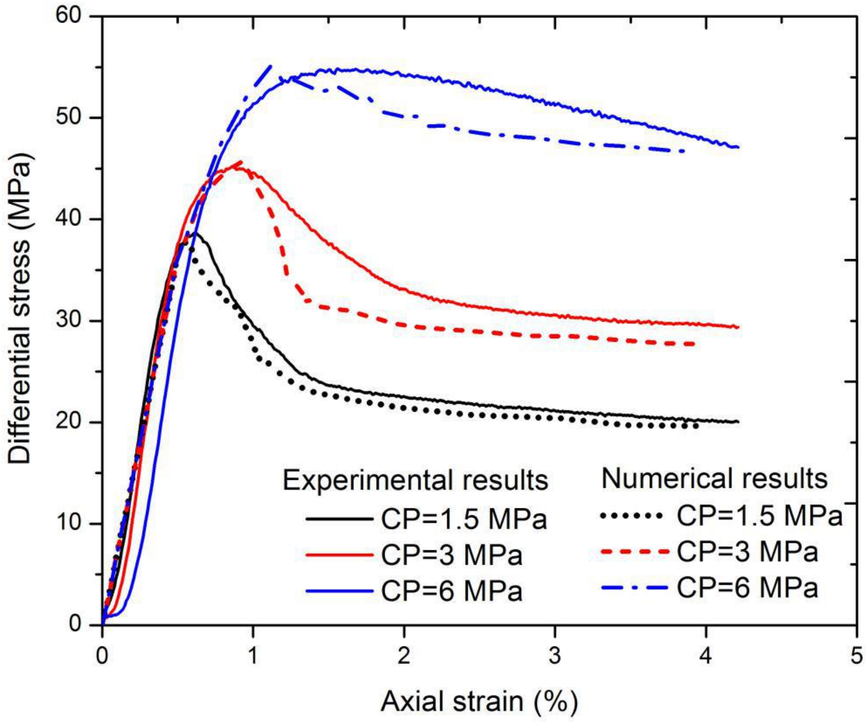
Differential stress (MPa)
Axial strain (%)
Experimental results
CP=1.5 MPa
CP=3 MPa
CP=6 MPa
Numerical results
CP=1.5 MPa
CP=3 MPa
CP=6 MPa
0
10
20
30
40
50
60
0
1
2
3
4
5

Fig 8

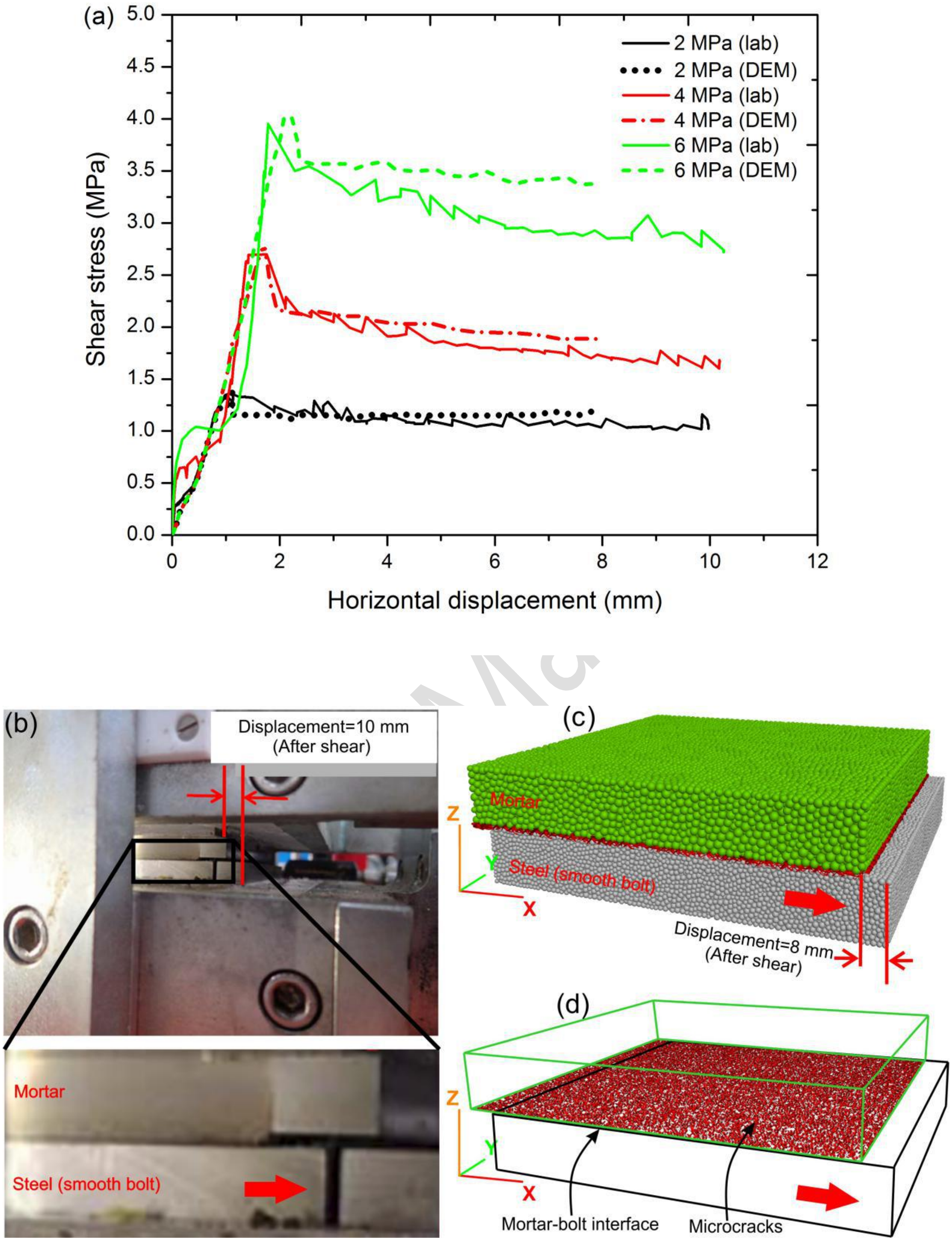

(a)
Shear stress (MPa)
Horizontal displacement (mm)
5.0
4.5
4.0
3.5
3.0
2.5
2.0
1.5
1.0
0.5
0.0
0
2
4
6
8
10
12
2 MPa (lab)
2 MPa (DEM)
4 MPa (lab)
4 MPa (DEM)
6 MPa (lab)
6 MPa (DEM)
(b)
Displacement=10 mm
(After shear)
Mortar
Steel (smooth bolt)
(c)
Mortar
Steel (smooth bolt)
Z
Y
X
Displacement=8 mm
(After shear)
(d)
Z
Y
X
Mortar-bolt interface
Microcracks

Fig 9

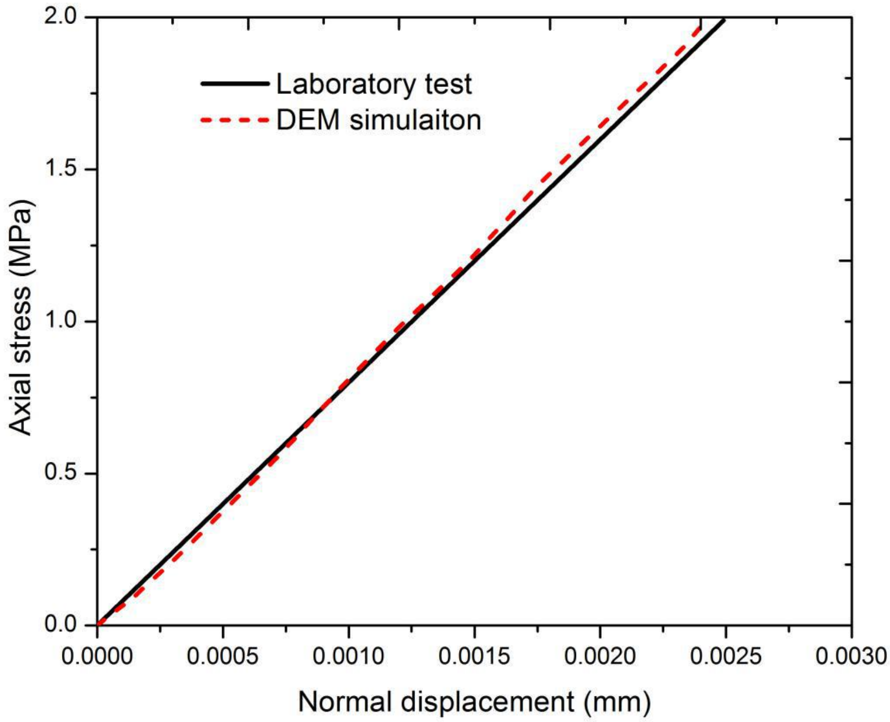

971

972 **Fig 10**

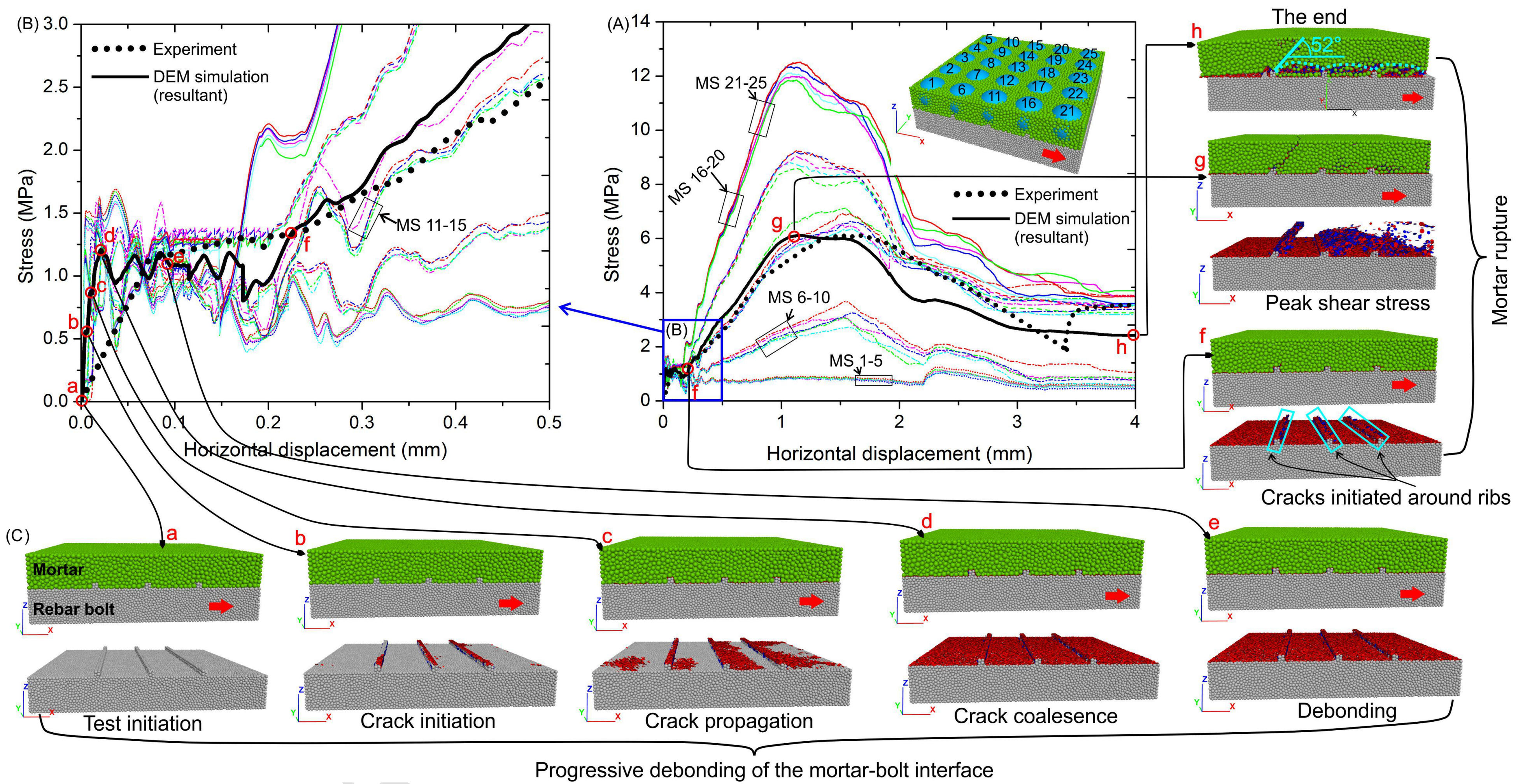

973

974 **Fig 11**

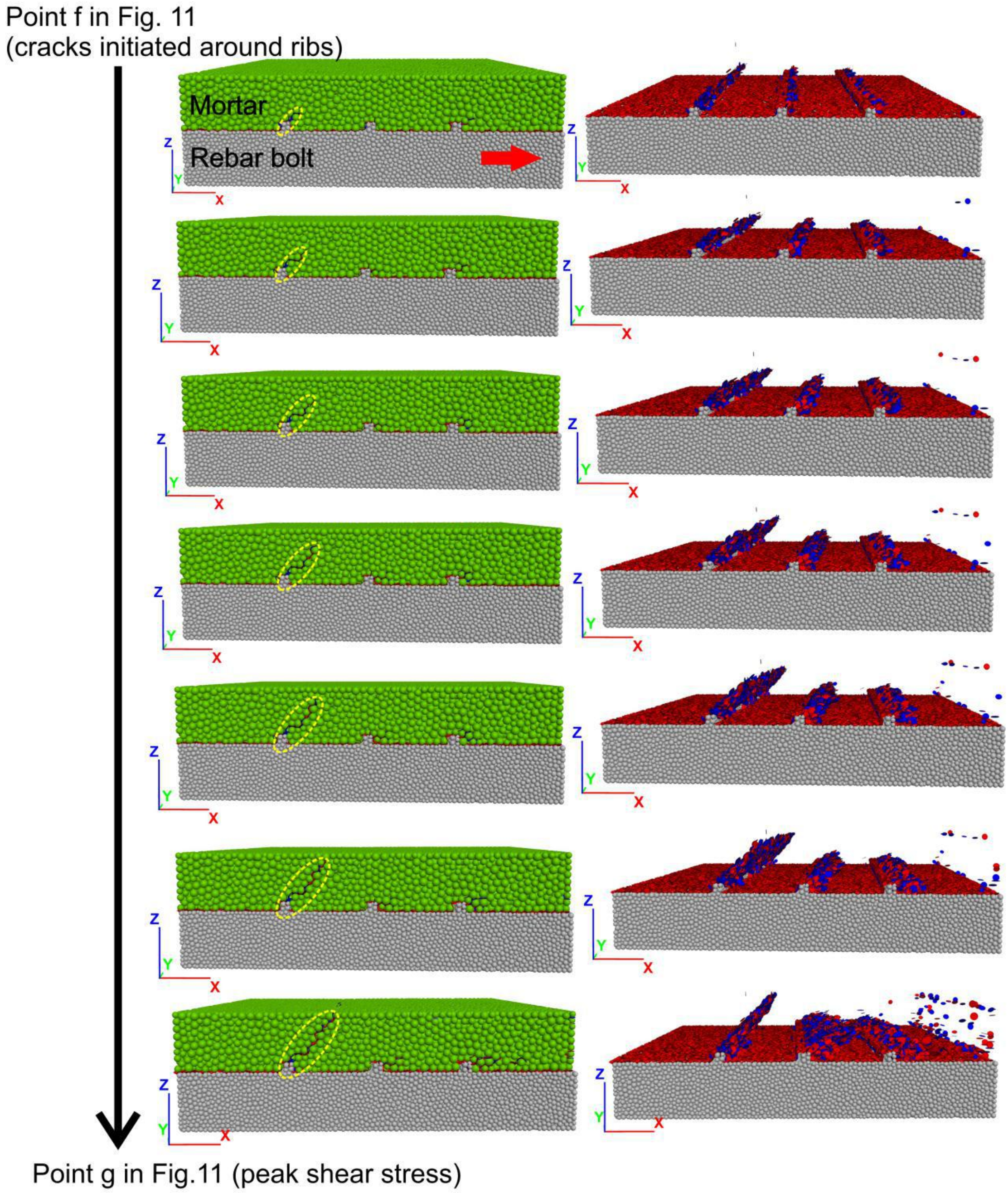

Point f in Fig. 11
(cracks initiated around ribs)
Mortar
Rebar bolt
Point g in Fig.11 (peak shear stress)

Fig 12

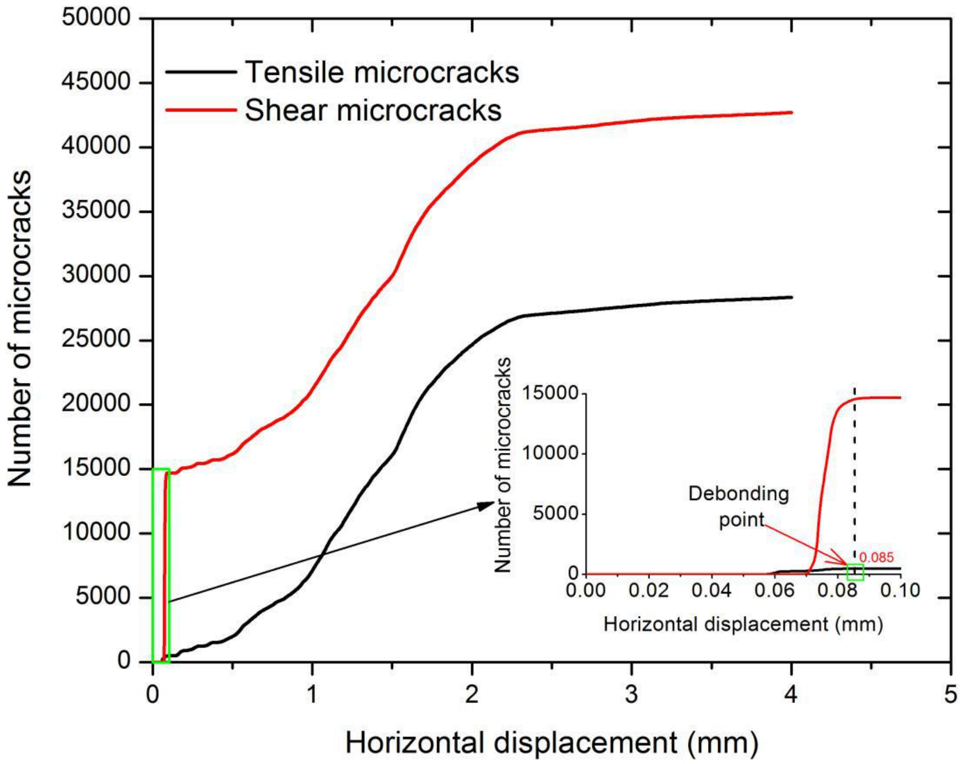

979

980 **Fig 13**

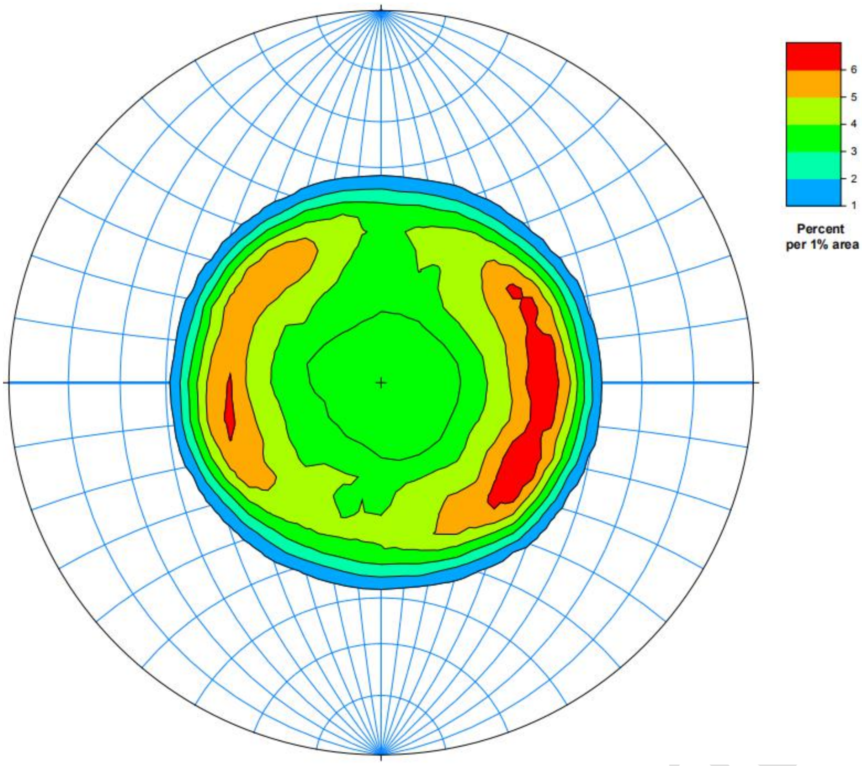

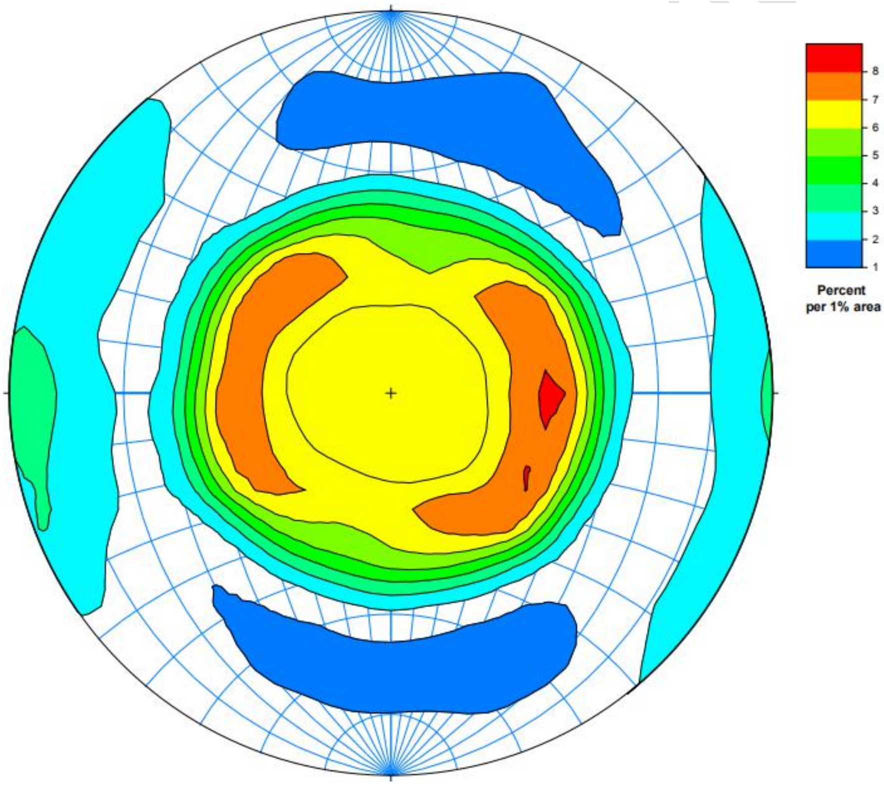

Fig 14

984

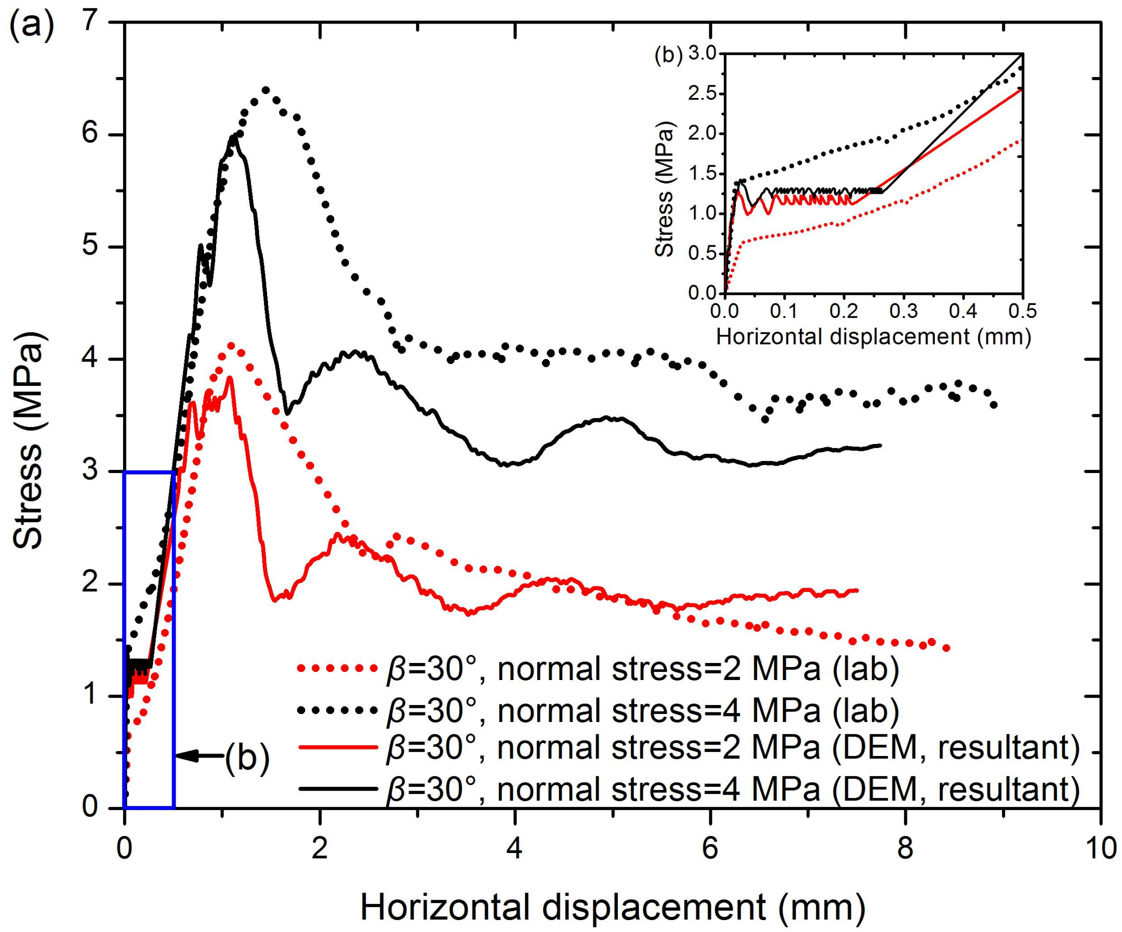

985 **Fig 15**

986

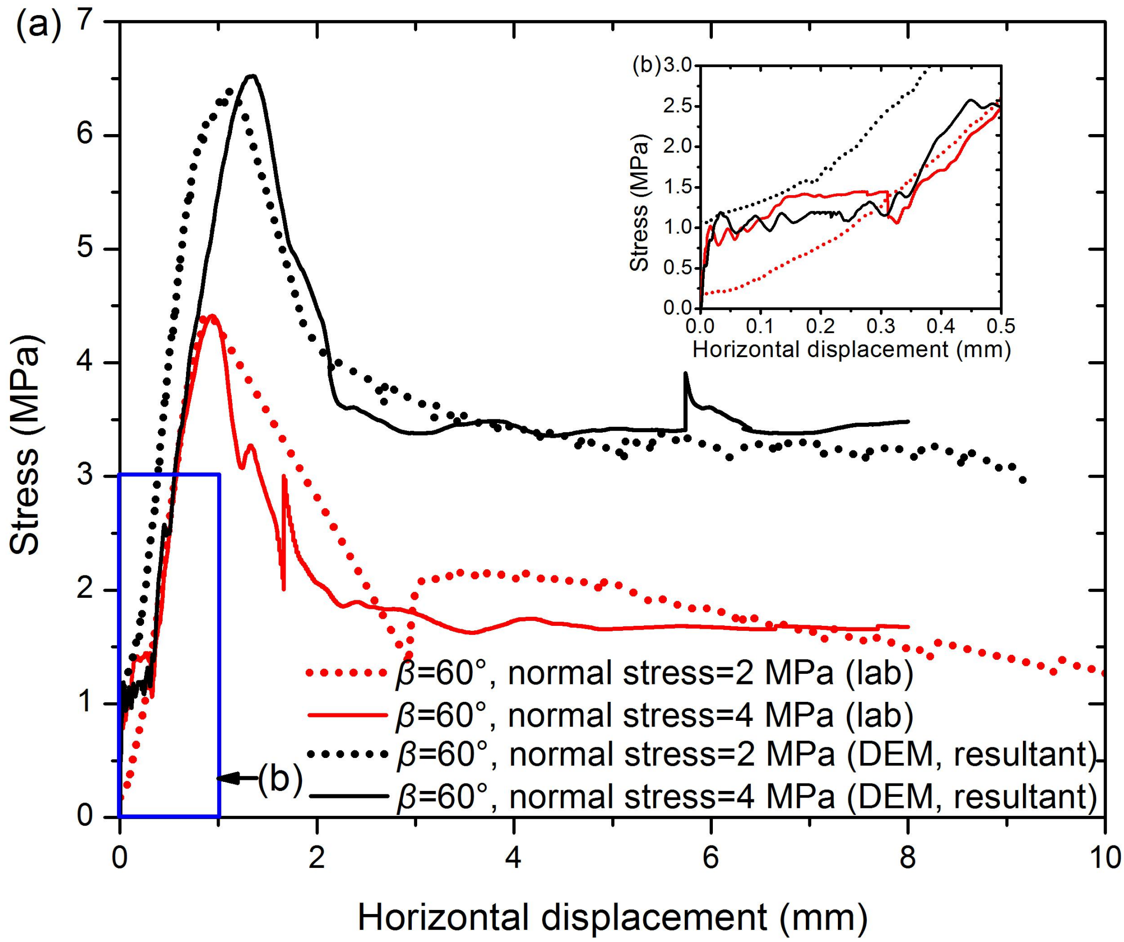

(a)
Stress (MPa)
Horizontal displacement (mm)
(b)
β=60°, normal stress=2 MPa (lab)
β=60°, normal stress=4 MPa (lab)
β=60°, normal stress=2 MPa (DEM, resultant)
β=60°, normal stress=4 MPa (DEM, resultant)

Fig 16

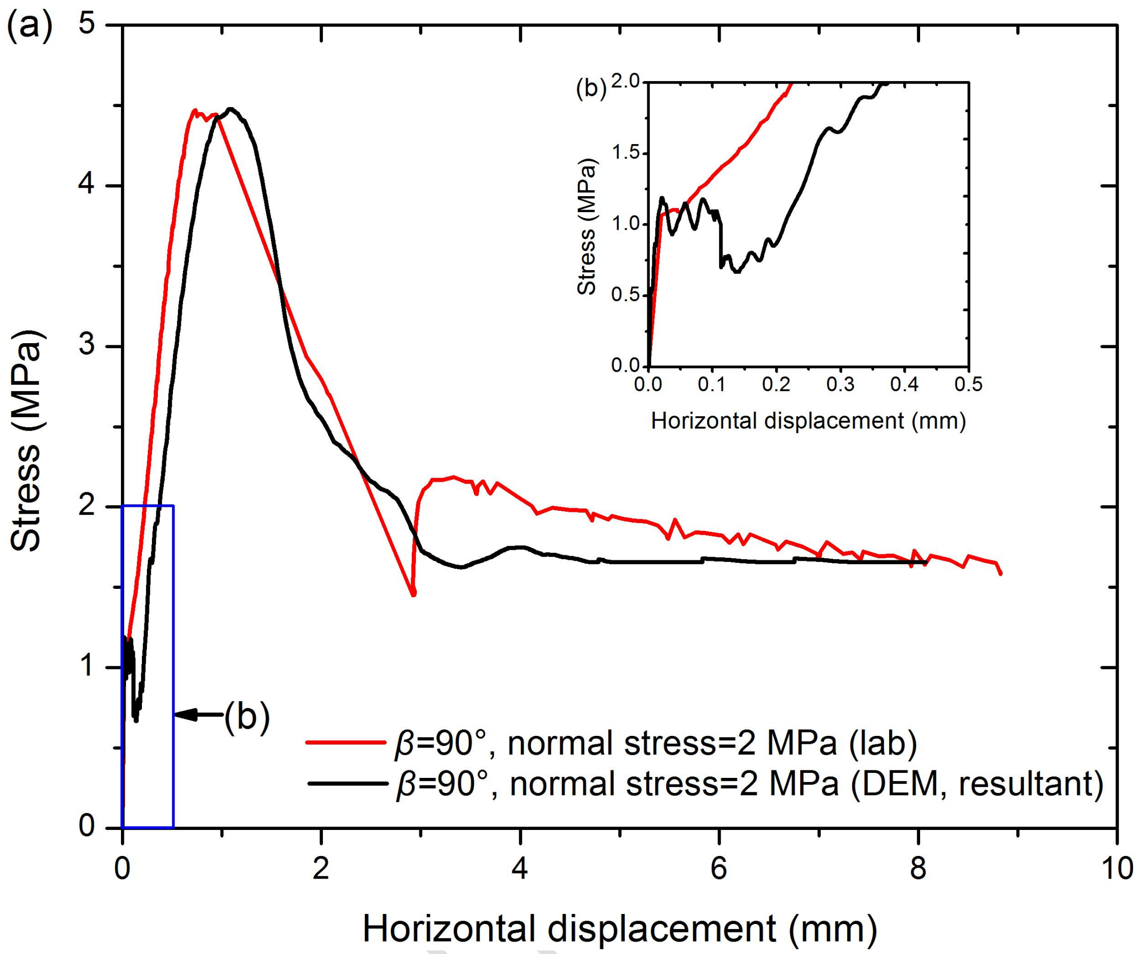

989

990 **Fig 17**

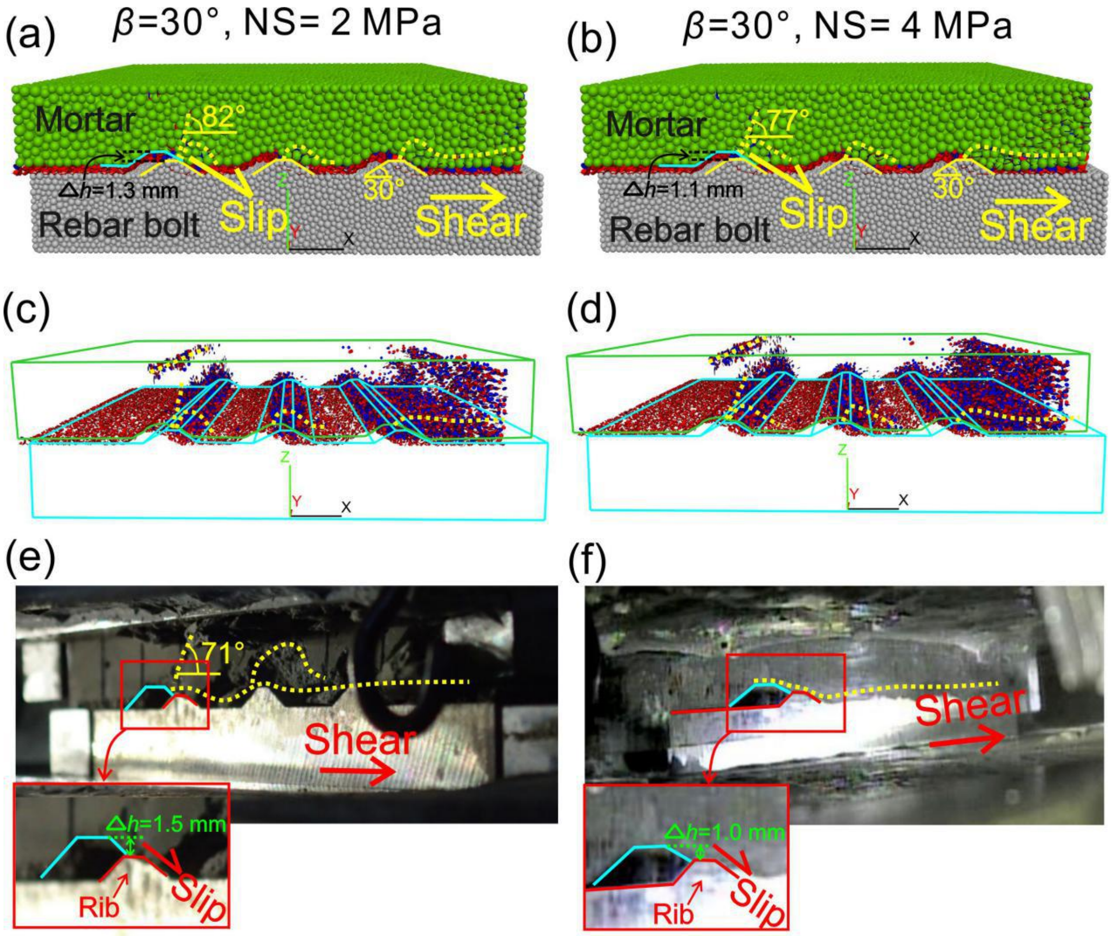

991
992 **Fig18**

993

994

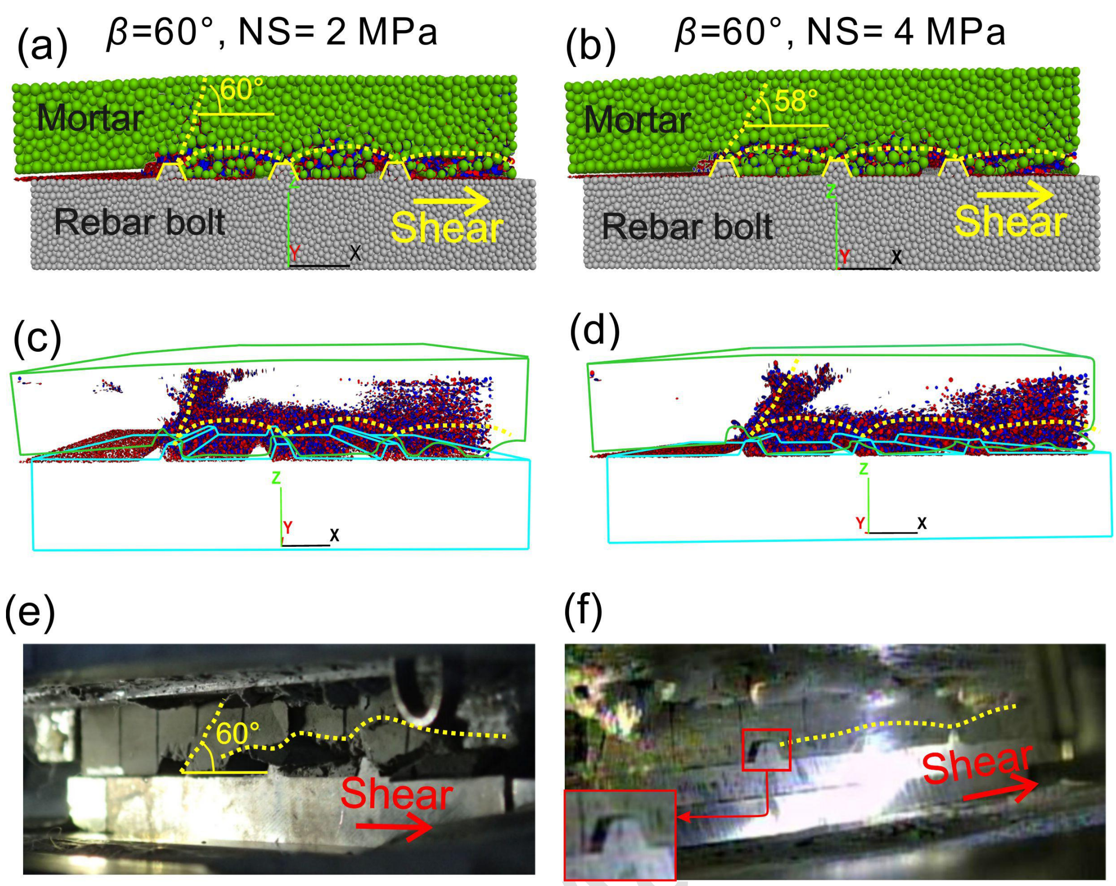
(a)
β=60°, NS= 2 MPa
60°
Mortar
Rebar bolt
Shear
(b)
β=60°, NS= 4 MPa
58°
Mortar
Rebar bolt
Shear
(c)
(d)
(e)
60°
Shear
(f)
Shear

Fig 19

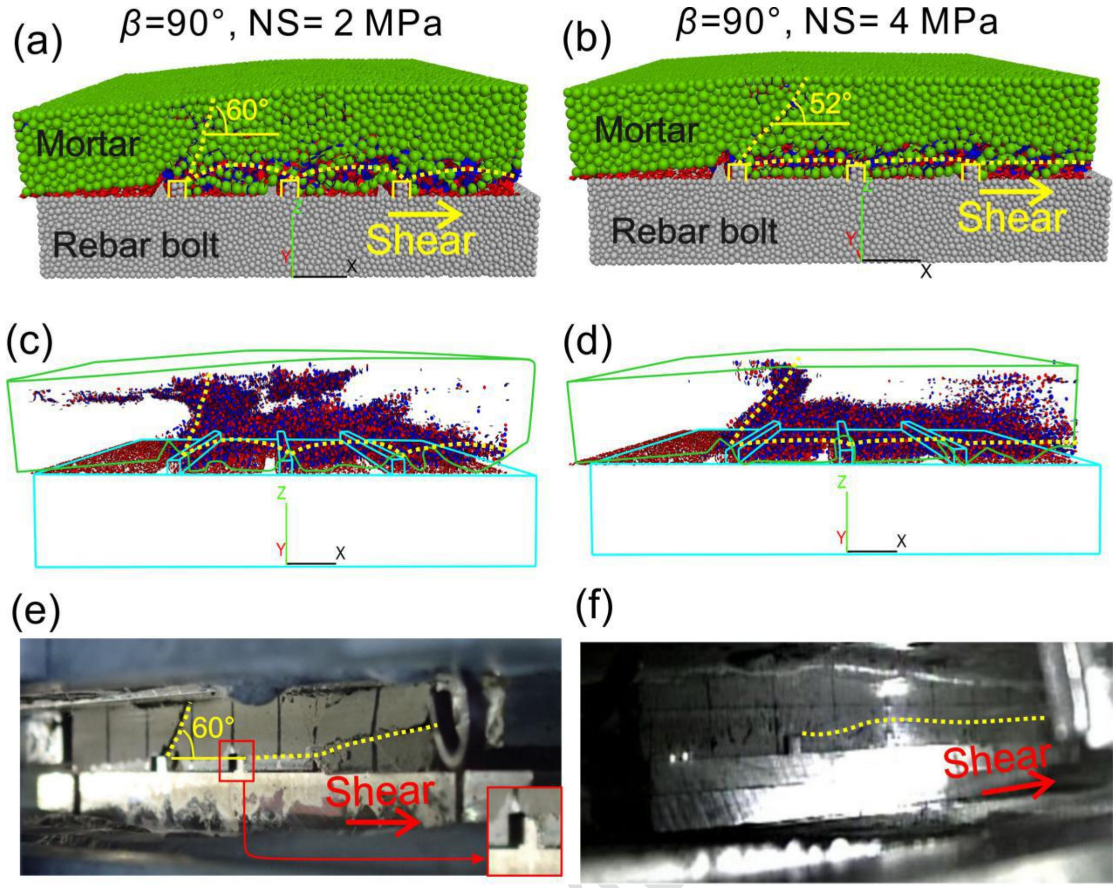

1002

1003 **Fig 20**

1004

1005

1006

1007

1008

1009 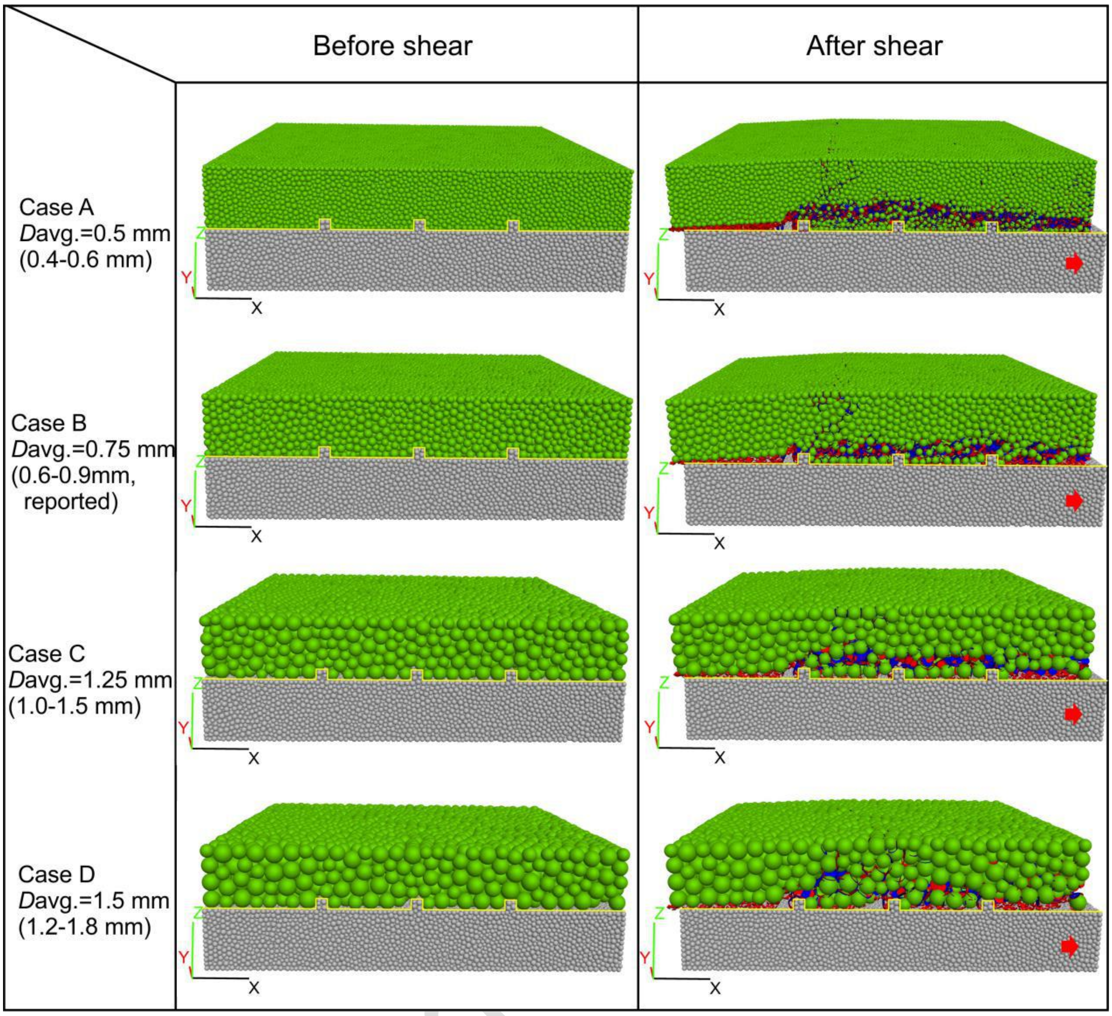

1010 **Fig 21**

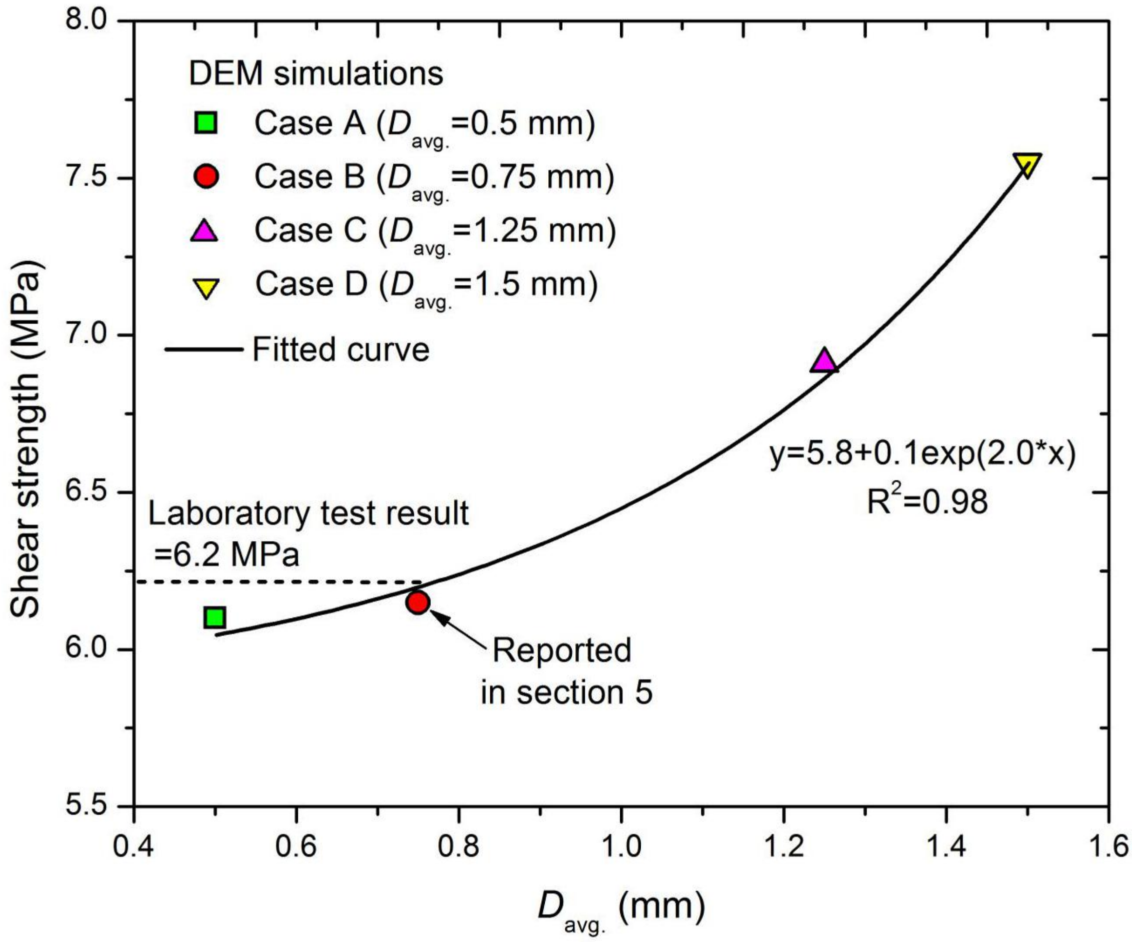
DEM simulations
Case A ($D_{avg.}$=0.5 mm)
Case B ($D_{avg.}$=0.75 mm)
Case C ($D_{avg.}$=1.25 mm)
Case D ($D_{avg.}$=1.5 mm)
Fitted curve
y=5.8+0.1exp(2.0*x)
R^2=0.98
Laboratory test result
=6.2 MPa
Reported
in section 5
Shear strength (MPa)
$D_{avg.}$ (mm)
8.0
7.5
7.0
6.5
6.0
5.5
0.4
0.6
0.8
1.0
1.2
1.4
1.6

Fig 22

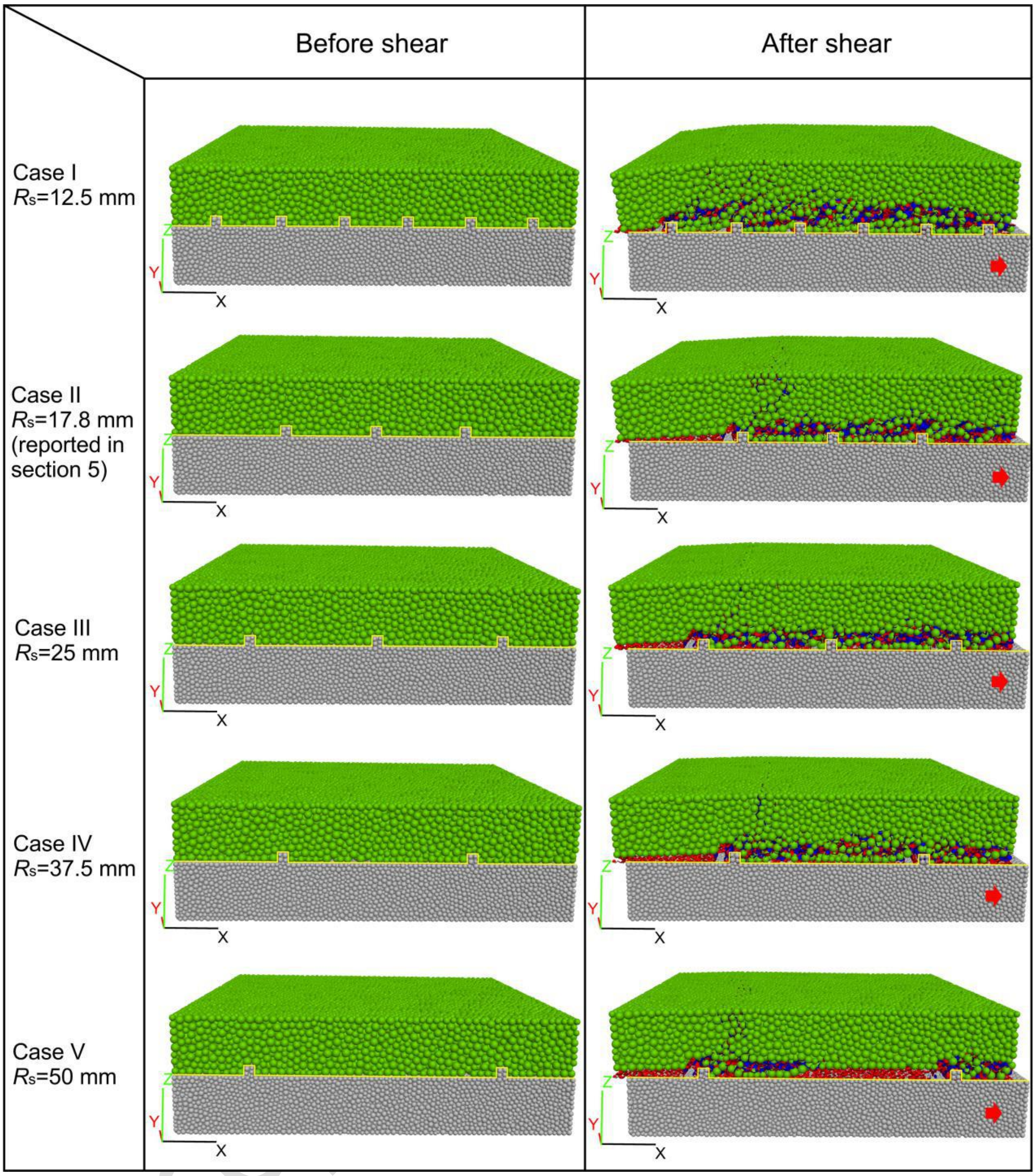

1015

1016 **Fig 23**

1017

1018

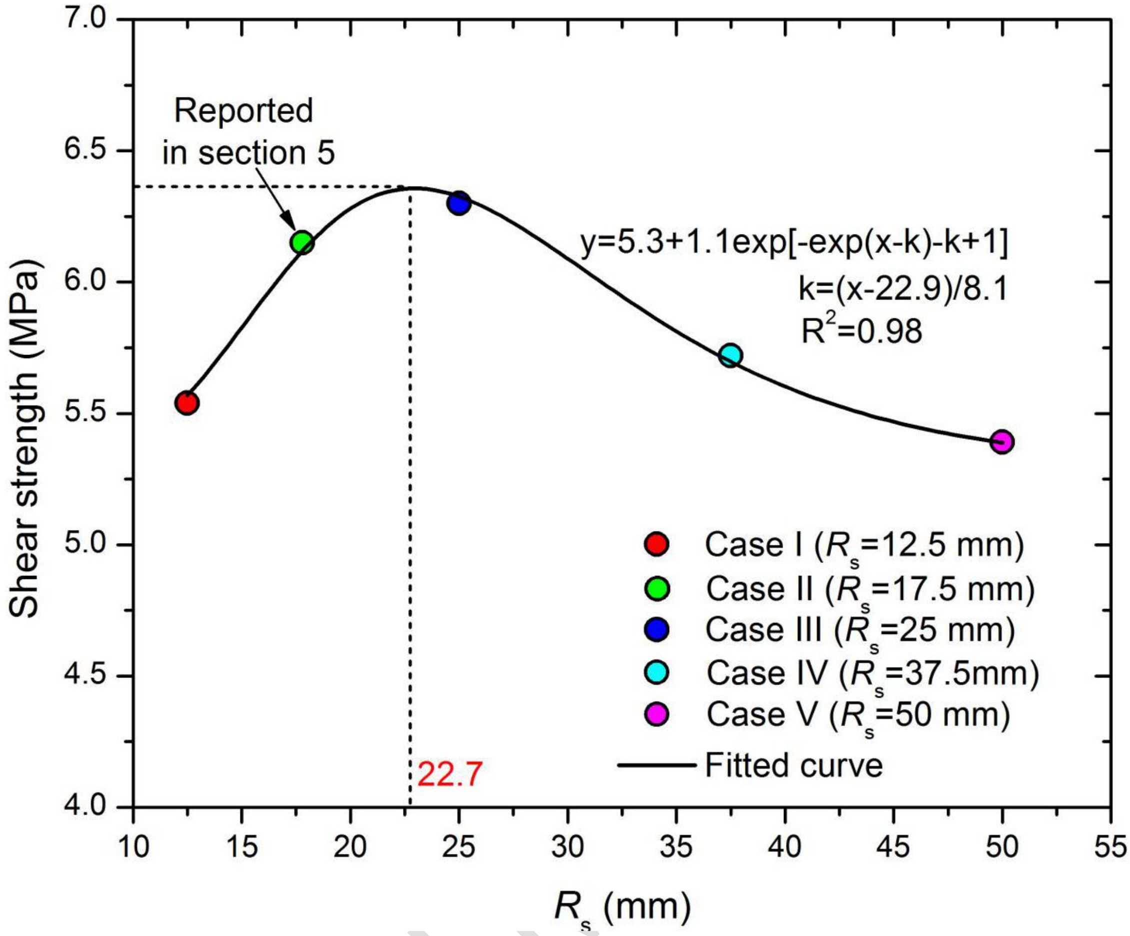
Reported
in section 5
y=5.3+1.1exp[-exp(x-k)-k+1]
k=(x-22.9)/8.1
R2=0.98
Shear strength (MPa)
7.0
6.5
6.0
5.5
5.0
4.5
4.0
22.7
10
15
20
25
30
35
40
45
50
55
Rs (mm)
Case I (Rs=12.5 mm)
Case II (Rs=17.5 mm)
Case III (Rs=25 mm)
Case IV (Rs=37.5mm)
Case V (Rs=50 mm)
Fitted curve

Fig 24

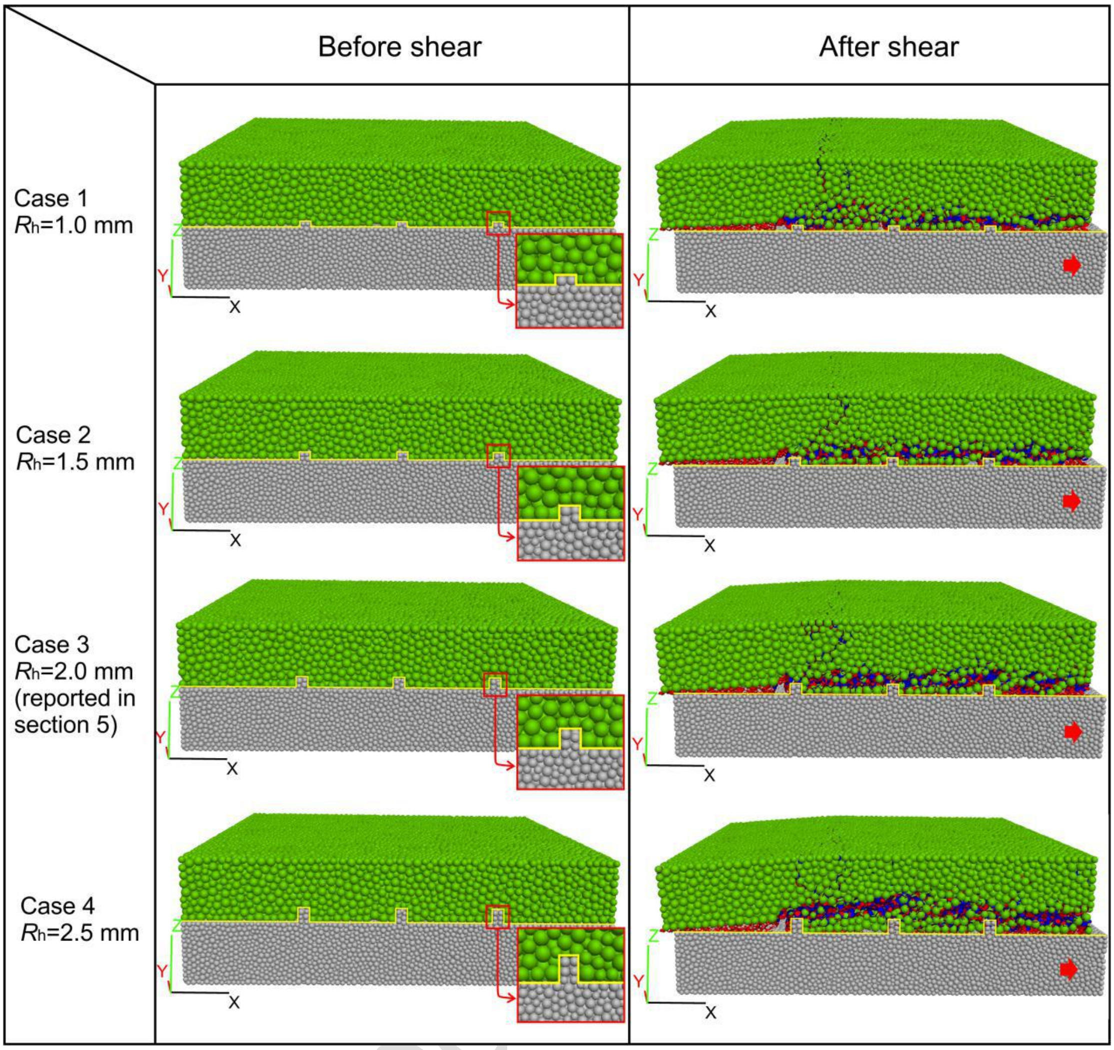

Before shear
After shear
Case 1
R_h=1.0 mm
Case 2
R_h=1.5 mm
Case 3
R_h=2.0 mm
(reported in
section 5)
Case 4
R_h=2.5 mm
Z
Y
X

Fig 25

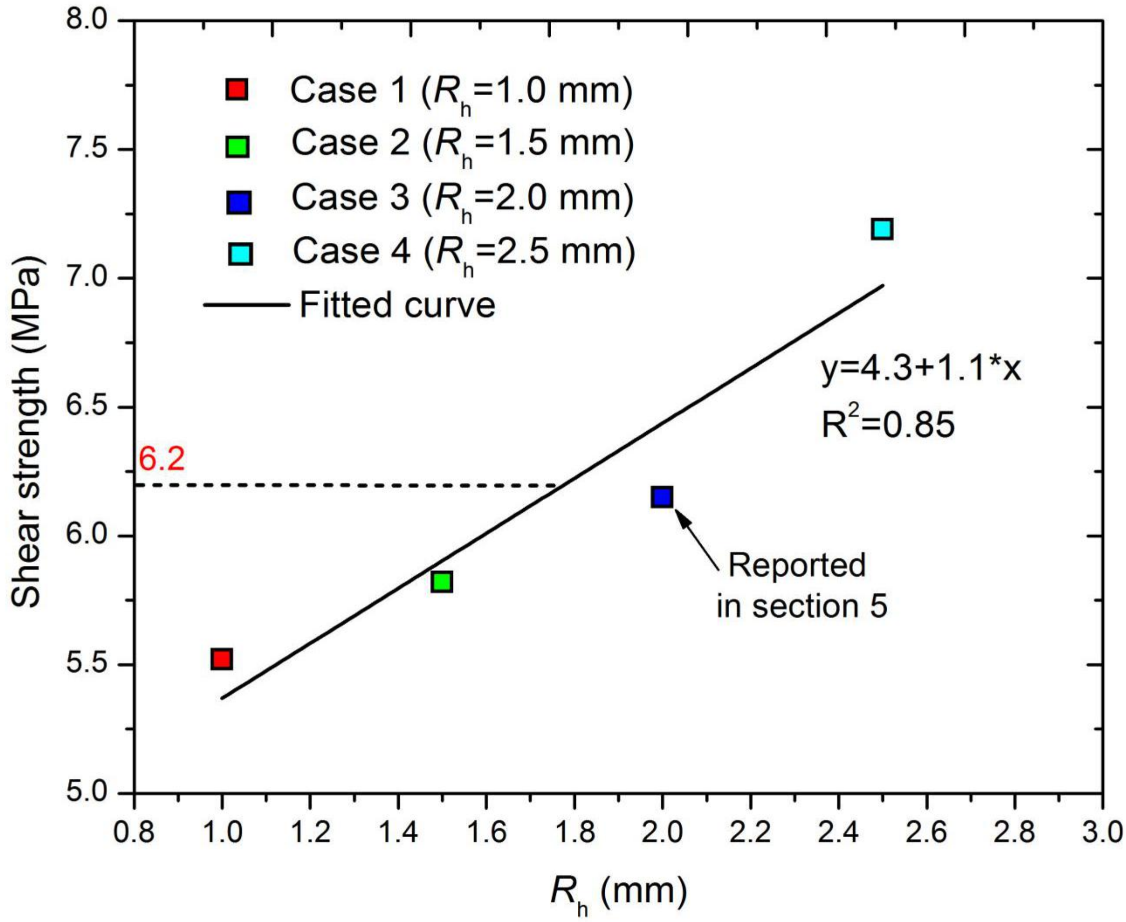
Case 1 (R_h=1.0 mm)
Case 2 (R_h=1.5 mm)
Case 3 (R_h=2.0 mm)
Case 4 (R_h=2.5 mm)
Fitted curve
y=4.3+1.1*x
R^2=0.85
6.2
Reported
in section 5
Shear strength (MPa)
R_h (mm)
8.0
7.5
7.0
6.5
6.0
5.5
5.0
0.8
1.0
1.2
1.4
1.6
1.8
2.0
2.2
2.4
2.6
2.8
3.0

Fig 26